# SIMULATING THE IMPACT OF DARK MATTER MODELS ON THE EPOCH OF REIONIZATION 21-cm SIGNAL

**M.Sc. Thesis**

By

**ANCHAL SAXENA**

**Discipline of Astronomy, Astrophysics and Space Engineering**

**INDIAN INSTITUTE OF TECHNOLOGY INDORE**

**June 2020**

# SIMULATING THE IMPACT OF DARK MATTER MODELS ON THE EPOCH OF REIONIZATION 21-cm SIGNAL

**M.Sc. Thesis**

*Submitted in partial fulfillment of the requirements for the awards of the degree*
***of***
**Master of Science**

by

**ANCHAL SAXENA**

**Discipline of Astronomy, Astrophysics and Space Engineering**

**INDIAN INSTITUTE OF TECHNOLOGY INDORE**

**June 2020**

# INDIAN INSTITUTE OF TECHNOLOGY INDORE

## CANDIDATE'S DECLARATION

I hereby certify that the work which is being presented in the thesis entitled **SIMULATING THE IMPACT OF DARK MATTER MODELS ON THE EPOCH OF REIONIZATION 21-cm SIGNAL** in the partial fulfillment of the requirements for the award of the degree of **MASTER OF SCIENCE** and submitted in the **DISCIPLINE OF ASTRONOMY, ASTROPHYSICS AND SPACE ENGINEERING, Indian Institute of Technology Indore**, is an authentic record of my own work carried out during the time period from JULY, 2019 to JUNE, 2020 under the supervision of Dr. Suman Majumdar, Assistant Professor, Indian Institute of Technology Indore.

The matter presented in this thesis has not been submitted by me for the award of any other degree of this or any other institute.

Anchal
21/06/2020

**Signature of the student with date**
**Anchal Saxena**

---

This is to certify that the above statement made by the candidate is correct to the best of my/our knowledge.

Suman Majumdar
21/06/2020

Signature of the Supervisor of M.Sc. thesis
**Dr. Suman Majumdar**

---

**Anchal Saxena** has successfully given his M.Sc. Oral Examination held on **12/06/2020**.

Suman Majumdar

Signature of the Supervisor of M.Sc. thesis
Dr. Suman Majumdar
Date: 21/06/2020

Suman Majumdar

Convener,DPGC
Date: 25/06/2020

Subhendu Rakshit

Signature of PSPC Member #1
Prof. Subhendu Rakshit
Date: 21/06/2020

Abhirup

Signature of PSPC Member #2
Dr. Abhirup Datta
Date: 24/06/2020

---

# ACKNOWLEDGEMENTS

First and foremost, I would like to express my sincere gratitude to my thesis supervisor Dr. Suman Majumdar for his patience, motivation, and enthusiasm for helping me to complete this work. Thank you for giving me the opportunity to work on this research project which has enabled me to draw out the best that is within me, and for supporting my career with your crucial suggestions.

I would like to extend my sincere thanks to Prof. Matteo Viel for collaborating in this project and for his insightful discussions and suggestions during different phases of this work. I also extend my thanks to Mohd. Kamran for the useful discussions and help during this work.

I also acknowledge the resources and facilities provided by the Discipline of Astronomy, Astrophysics and Space Engineering at the Indian Institute of Technology Indore.

# Abstract

The nature of dark matter sets the timeline for the formation of first collapsed halos and thus affects the sources of reionization. In this work[1], we consider two different models of dark matter: cold dark matter (CDM) and thermal warm dark matter (WDM), and study how they impact the epoch of reionization (EoR) and its 21-cm observables. Using a suite of simulations, we find that in the WDM scenarios, the structure formation on small scales gets suppressed resulting in a smaller number of low mass dark matter halos compared to the CDM scenario. Assuming that the efficiency of sources in producing ionizing photons remain the same, this leads to a lower number of total ionizing photons produced at any given cosmic time and thus in a delay in the reionization process. We also find visual differences in the neutral hydrogen (H I) topology and in 21-cm maps in case of the WDM compared to the CDM. However, differences in the 21-cm power spectra, at the same neutral fraction, are found to be small. Thus, we focus on the non-Gaussianity in the EoR 21-cm signal, quantified through its bispectrum. We find that the 21-cm bispectra (driven by the H I topology) are significantly different in WDM models when compared with CDM, even for same mass averaged neutral fractions. This establishes that the 21-cm bispectrum is a unique and promising way to differentiate between different dark matter models, and can be used to constrain the nature of the dark matter in the future EoR observations.

[1]A significant portion of this thesis is adapted from the article: "Impact of dark matter models on the EoR 21-cm signal bispectrum"; Anchal Saxena, Suman Majumdar, Mohd. Kamran, Matteo Viel; Submitted in the Monthly Notices of the Royal Astronomical Society. arXiv:2004.04808

# LIST OF PUBLICATIONS

1. Anchal Saxena, Suman Majumdar, Mohd. Kamran, Matteo Viel; *Impact of dark matter models on the EoR 21-cm signal bispectrum*. Accepted for publication in the Monthly Notices of the Royal Astronomical Society. arXiv:2004.04808

# Contents

# List of Figures

# List of Tables

# Acronyms

**CD** Cosmic Dawn.

**CDM** Cold Dark Matter.

**CMB** Cosmic Microwave Background.

**DARE** Dark Ages Radio Explorer.

**EDGES** Experiment to Detect the Global EoR Signature.

**EoR** Epoch of Reionization.

**GIMP** Gravitationally Interacting Massive Particle.

**GMRT** Giant Metrewave Radio Telescope.

**IGM** Inter-Galactic Medium.

**LOFAR** LOw Frequency ARray.

**MWA** Murchison Widefield Array.

**PAPER** Precision Array for Probing the Epoch of Reionization.

**SARAS** Shaped Antenna measurement of the background RAdio Spectrum.

**SKA** Square Kilometre Array.

**WDM** Warm Dark Matter.

**WIMP** Weakly Interacting Massive Particle.

# Chapter 1

# Introduction

Cosmology is the study of the evolutionary history of the Universe, and one crucial missing chapter in this history is the Cosmic Dawn and Epoch of Reionization. This was the period when the first sources of light in the Universe were formed, and these and subsequent population of sources emitted the high energy X-ray and UV radiation, which in turn heated up and reionized the intergalactic medium (see e.g. Barkana et al. 2001; Furlanetto, Oh, et al. 2006, for reviews). This is the period in cosmic history when the Universe has witnessed the formation of the first bound structures. Thus, the CD-EoR has significant implications on the large scale structures that we see around us today.

After the cosmological recombination, the Universe went into the dark ages, so named because the luminous sources including the stars and galaxies that we observe today had yet to form. During these dark ages, the density fluctuations in the matter distribution grew, and after reaching a threshold, the matter collapsed to make the first bound objects. The nature of dark matter sets the timeline of formation and the characteristics of these first bound objects, which were the hosts for the first sources of light. Thus, it is essential to analyse the impact of different dark matter models on the observables from the Cosmic Dawn and EoR. The subsequent natural question that arises is whether one can use the differences in these observables, estimated for different dark matter models, in order to constrain the nature of dark matter. The present observational probes that allow us to have a peak in this epoch are the absorption spectra of high redshift quasars (Boera et al. 2019; Loeb et al. 2001; White et al. 2003) and the Thompson scattering optical depth of the Cosmic Microwave Background Radiation photons (Kaplinghat et al. 2003; Komatsu et al. 2011). However, these indirect probes provide very limited and weak constraints on the CD-EoR. The H I 21-cm line, which arises due to the hyperfine splitting of the ground state of the neutral hydrogen, is a direct and most promising probe to study this period. Motivated by this, a large number of radio interferometers, including the GMRT[1] (Paciga et al. 2013), LOFAR[2] (Ghara et al. 2020; Mertens et al. 2020), MWA[3] (Barry et al. 2019; Li et al. 2019) and PAPER[4] (Kolopanis et al. 2019) are attempting a statistical detection of this signal using the power spectrum statistic. In parallel, there is a complementary approach to detect the sky averaged global 21-cm signal from the CD-EoR using experiments e.g. the EDGES[5] (Bowman et al. 2018), DARE[6] (Burns et al. 2017), and SARAS[7] (Singh et al. 2018). The next-generation interferometers like the SKA[8] (Koopmans et al. 2015; Mellema et al. 2015) are expected to see a giant leap in the sensitivity, which will enable them to make tomographic images of the H I distribution across cosmic time.

The nature of the dark matter is mostly unknown to us. We can classify the dark matter into cold, warm, and hot categories based on the free streaming length scale of the dark matter particles (see Schneider 2012, and references therein). The ΛCDM cosmology is consistent with several observations at large scales, including the observations of Lyman-$\alpha$ forest at small and medium scales, clusters and CMB anisotropies. However, some discrepancies between the theory and observations arise at small scales $\leq$ 1.0 Mpc. Some of these are labeled as the too-big-to-fail problem, the core-cusp problem, satellite abundance, and galaxy abundance in mini-voids (see Bullock et al. 2017; Primack 2009; Weinberg et al. 2015, for

[1] http://www.gmrt.ncra.tifr.res.in/
[2] http://www.lofar.org/
[3] http://www.mwatelescope.org/
[4] http://eor.berkeley.edu/
[5] https://www.haystack.mit.edu/ast/arrays/Edges/
[6] https://www.colorado.edu/dark-ages-radio-explorer/
[7] http://www.rri.res.in/DISTORTION/saras.html
[8] https://www.skatelescope.org/

more details). These issues may be resolved either by invoking astrophysical baryonic processes or by assuming the dark matter to be warm instead of cold. Cosmology and especially structure formation and evolution can thereby be a suitable probe for studying such dark sectors (Schneider 2012; Viel, Becker, et al. 2013).

Two potential candidates for the warm dark matter are sterile neutrinos and gravitinos, both of which require the extensions of the standard model of particle physics (Boyarsky et al. 2019; Dodelson et al. 1994; Viel, Lesgourgues, et al. 2005). However, in this work, we consider a thermal relic to be the candidate for the WDM. Unlike sterile neutrinos, this candidate is probably less motivated but easier to simulate given the fact that its transfer function has been more studied by several authors, also in terms of non-linear structure formation. Several studies have constrained the WDM particle mass using galaxy luminosity function of high redshift galaxies and Lyman-$\alpha$ forest data (P. S. Corasaniti et al. 2017; Dayal et al. 2017; Kennedy et al. 2014; Safarzadeh et al. 2018) and found a robust lower bound on the thermal warm dark matter particle mass to be $\geq 2$ keV. Recent Lyman-$\alpha$ forest power spectrum analyses point to somewhat tighter limits $> 3.5$ keV at the $2\sigma$ C.L. (Iršič et al. 2017). However, for the purposes of the present work, it is appropriate to investigate the values of the thermal masses that are also in principle already ruled out by other observables.

In this work, we consider the standard CDM model and thermal warm dark matter (WDM) with masses of the thermal relic of 2 and 3 keV. Investigations of the structure formation processes in the WDM scenario and especially at high redshifts have been performed by e.g. Maio et al. 2015 (and references therein). Recently, reionization has been studied in the warm dark matter models or extensions of the standard CDM scenario by several authors (Carucci, P.-S. Corasaniti, et al. 2017; Carucci, Villaescusa-Navarro, et al. 2015; Das et al. 2018; Dayal et al. 2017; Gao et al. 2007; Lapi et al. 2015; Lovell et al. 2014; Sitwell et al. 2014; Villanueva-Domingo et al. 2018). These studies have focused on the 21-cm power spectrum and found the differences in the 21-cm power spectrum to be significantly small between different models of the dark matter, and probably not large enough to be detectable by the first generation of radio interferometers.

However, the 21-cm power spectrum can provide a complete description of a signal only if it is a Gaussian random process in nature. Whereas, the EoR 21-cm signal is highly non-Gaussian, specifically during the intermediate and later stages of reionization [see also (Pillepich et al. 2007)]. The power spectrum, therefore, can not capture this non-Gaussian feature of the signal. The effort to differentiate between different models of dark matters using the 21-cm power spectrum will not be optimal as it does not capture the non-Gaussian information present in the signal. To capture this evolving non-Gaussianity, one would need to use a higher-order statistic, the bispectrum, which is the Fourier equivalent of the 3-point correlation function. Recently, the CD-EoR 21-bispectrum has been investigated using both analytical models and numerical simulations, see e.g. Bharadwaj and Pandey 2005; Hutter et al. 2020; Majumdar, Pritchard, et al. 2018; Shimabukuro et al. 2016; Catherine A Watkinson et al. 2018. These authors have independently confirmed that there are two major sources of non-Gaussianity in this signal, they are the matter density fluctuations and the neutral fraction fluctuations. In this work, we aim to quantify the differences in the observables of the CD-EoR 21-cm signal for different dark matter models. Through this analysis, we would like to identify the optimal statistics that can be used to distinguish between different dark matter models and their signature on the CD-EoR 21-cm signal.

This thesis is organized as follows: In chapter 2, we discuss the formation of structures in different dark matter models followed by our approach to simulate these dark matter cosmologies. In chapter 3, we concisely describe our semi-numerical approach to simulate the redshifted 21-cm signal and methods to estimate different statistics out of it. Chapter 4 describes our results. In chapter 5, we summarize our findings.

Throughout this work, we have used the values of cosmological parameters as $\Omega_{\mathrm{m}} = 0.308$, $\Omega_{\mathrm{b}} = 0.048$, $\Omega_{\Lambda} = 0.692$, $h = 0.678$ and $\sigma_8 = 0.829$ (Planck Collaboration et al. 2016).

# Chapter 2

# Structure formation in different dark matter models and the EoR 21-cm signal as an observational probe

Dark matter is abundant in the Universe. There are several observational pieces of evidence for the existence of the dark matter, including galaxy rotation curves, gravitational lensing, cosmic microwave background, and the baryonic acoustic oscillation measurements etc. However, its nature remains one of the major mysteries of the Universe. Most of the dark matter is thought to be composed of some yet undiscovered subatomic particles which are non-baryonic in nature. The primary proposed candidate for the dark matter is a Weakly Interacting Massive Particle (WIMP), having mass in range 10 GeV - TeV (see Arcadi et al. 2018; Roszkowski et al. 2018, for reviews). These are the hypothetical particles that interact through gravity and any force, whose interaction strength is less than or comparable to the weak nuclear force. This force potentially does not belong to the standard model itself.

Dark matter interacts dominantly via gravity with the ordinary matter and also with itself. Several hypothetical particles have been proposed as the non-baryonic candidates for the dark matter, including WIMPs, axions, GIMPs, sterile neutrinos, supersymmetric particles, etc. (Bergström 2009; Bertone et al. 2005; Feng 2010). In the next section, we discuss the nature of the currently favored ΛCDM model and its inconsistencies with the observations on small scales.

## 2.1 ΛCDM model and its discrepancies on small scales

According to the currently favored ΛCDM model, the dark matter candidate is a neutralino, which is the lightest stable particle in supersymmetry. These particles have a mass of around 100 GeV with negligible thermal velocities. These velocities are too low to affect the formation of structures on the galactic scales, and so, we have hierarchical structure formation in cold dark matter scenario (Diemand et al. 2011; Frenk et al. 2012; Press et al. 1974; Yoshida, Abel, et al. 2003). ΛCDM model is consistent with plenty of observations, including the large scale structures of galaxies and galaxy clusters except for the discrepancies which arise at relevant small scales $\leq 1.0$ Mpc. Here, we summarize some of these issues, which are discussed in Primack (2009) and Del Popolo et al. (2017).

1. **Core-cusp problem**: Simulations of structure formation in the CDM model predicts a density profile of the form $\rho(r) \sim r^{-n}$ where $n \sim 1$ in the galaxy cores [Figure 1 of Del Popolo et al. (2017)], which is inconsistent with the observed flat profiles of the dwarf galaxies and the galaxies having low brightness.

2. **Missing satellites problem**: The number of subhalos predicted by the N-body simulations is more than the observed satellite galaxies. A possible explanation would be that these galaxies are too faint to be observed.

3. **Galaxy abundance in mini-voids**: Most of the dwarf galaxies are observed to be located near the bright and large galaxies. Simulations of the CDM predict a larger abundance of such dwarf galaxies than the observed.

All of the above issues arise on small scales $\leq 1.0$ Mpc, so the key is to find a mechanism that suppresses the formation of structures on such small scales. In the next section 2.2, we discuss how the warm dark matter suppresses the formation of structure on small scales. So, in principle, these issues may get resolved by assuming the dark matter to be warm instead of cold.

## 2.2 Impact of dark matter models on structure formation

Dark matter can be classified into cold, warm, and hot categories. This classification is done according to the free streaming scale of the dark matter particles (Abazajian et al. 2001; Bode et al. 2001; Kolb et al. 1990; Schneider, Smith, and Reed 2013; Smith et al. 2011). In the early Universe, primordial density perturbations on scales smaller than this length scale get damped because dark matter particles at these scales stream out from the overdense to the underdense regions. However, the density fluctuations on the scales larger than this scale remain unaffected.

### 2.2.1 Free streaming scale of the dark matter particles

We can define the free streaming length $\lambda_{\mathrm{FS}}$ as the length traversed by a dark matter particle before the density perturbations start to grow significantly. It can be calculated as

$$\lambda_{\mathrm{FS}} = \int_0^{t_{\mathrm{MRE}}} \frac{v(t)\,\mathrm{d}t}{a(t)} = \int_0^{t_{\mathrm{NR}}} \frac{c\,\mathrm{d}t}{a(t)} + \int_{t_{\mathrm{NR}}}^{t_{\mathrm{MRE}}} \frac{v(t)\,\mathrm{d}t}{a(t)}\,, \tag{2.1}$$

where $t_{\mathrm{MRE}}$ represents the epoch of matter-radiation equality, and $t_{\mathrm{NR}}$ represents the onset of non-relativistic behavior of dark matter particles. Also, we have made use of the fact that in relativistic domain, $v(t) \sim c$. In the non-relativistic regime as $v(t) \sim a(t)^{-1}$ and during the radiation dominated era, $a(t) \propto t^{1/2}$, so Equation (2.1) leads to

$$\lambda_{\mathrm{FS}} \sim \frac{2ct_{\mathrm{NR}}}{a_{\mathrm{NR}}} \left[1 + \log\left(\frac{a_{\mathrm{MRE}}}{a_{\mathrm{NR}}}\right)\right]. \tag{2.2}$$

So, if the dark matter particles become non-relativistic later, thereby increasing the $t_{\mathrm{NR}}$, they will lead to a larger free streaming scale $\lambda_{\mathrm{FS}}$.

These erased initial perturbations will cause the formation of a halo to get suppressed. The mass of such haloes can be calculated as

$$M_{\mathrm{FS}} = \frac{4}{3}\pi \left(\frac{\lambda_{\mathrm{FS}}}{2}\right)^3 \bar{\rho}\,. \tag{2.3}$$

In cold dark matter, the dark matter particles become non-relativistic already at the time of decoupling $t_{\mathrm{NR}} \sim t_{\mathrm{dec}}$, leading to a very small free streaming length. Hence, we have a bottom-up scheme for the formation of structure in the CDM model with galaxies forming first and galaxy clusters later. Several dark matter simulations confirm this. However, this model is inconsistent with the observations on small scales.

We can consider the other extreme also where the transition of the dark matter particles from being relativistic to being non-relativistic takes place around the matter radiation equality (i.e. $t_{\mathrm{NR}} \sim t_{\mathrm{MRE}}$). This leads to a very large free streaming length. This model predicts a top-down scheme for the formation of structure even at large length scales as confirmed by Bode et al. (2001); Brandbyge et al. (2017), where clusters and superclusters were formed first, which later fragment into the galaxies, which is inconsistent with the observations.

In warm dark matter scenario, the particles become non-relativistic later compared to the CDM model and the $t_{\mathrm{NR}}$ lies somewhere in between $t_{\mathrm{dec}} < t_{\mathrm{NR}} < t_{\mathrm{MRE}}$. Thus, the dark matter particles' free streaming scale in the WDM model is larger compared to the CDM model. It results in a bottom-up structure formation at scales greater than $\lambda_{\mathrm{FS}}$ and a top-down structure formation at scales less than $\lambda_{\mathrm{FS}}$ leading to a suppressed formation of structures at small scales (Bode et al. 2001; Schneider, Smith, Macciò, et al. 2012).

### 2.2.2 Evolution of Jeans mass through cosmic history

The impact that the free streaming of the dark matter particles have on structure formation can be understood by studying how the Jeans mass evolves through cosmic history (Schneider 2012; Schneider, Smith, and Reed 2013). To describe the growth of perturbations, one can consider the small perturbations on top of the uniform background density of the dark matter particles. We can define these perturbation as

$$\delta(\mathbf{r}, t) = \frac{\rho(\mathbf{r}, t) - \bar{\rho}(t)}{\bar{\rho}(t)}, \tag{2.4}$$

where $\rho(\mathbf{r}, t)$ is the matter density at position $\mathbf{r}$ at time $t$ and $\bar{\rho}(t)$ is the background matter density at time $t$ with the peculiar velocity of particles as $\mathbf{v} = \mathbf{u} - H\mathbf{r}$. The description of this fluid is given by the continuity and Euler equation [Equation (2.5) and (2.6) respectively].

$$\frac{\partial \delta}{\partial t} + \frac{1}{a}\nabla \cdot [(1+\delta)\mathbf{v}] = 0 \tag{2.5}$$

$$\frac{\partial v}{\partial t} + H\mathbf{v} + \frac{1}{a}(\mathbf{v}\cdot\nabla)\mathbf{v} = -\frac{1}{a}\nabla\phi - \frac{1}{a\bar{\rho}}\nabla(\delta p) \tag{2.6}$$

The gravitational potential can be calculated using the Poisson equation as

$$\nabla^2\phi = 4\pi G a^2 \bar{\rho}\delta\,. \tag{2.7}$$

Thus, the linear evolution of these matter density fluctuations is described as [by combining Equations (2.5), (2.6) and (2.7)]

$$\frac{\partial^2 \delta}{\partial t^2} + 2\frac{\dot{a}}{a}\frac{\partial \delta}{\partial t} = \frac{\sigma^2}{a^2}\nabla_{\mathrm{x}}^2\delta + 4\pi G\bar{\rho}(t)\delta\,. \tag{2.8}$$

For convenience, we use the Fourier representation to describe the matter density field where the strength of fluctuations on a length scale $\lambda = 2\pi/k$ is given by the amplitude of that $k$-mode.

$$\delta(\mathbf{x}, t) = \int \mathrm{d}^3k\, \delta_{\mathbf{k}}(t) e^{i\,\mathbf{k}\cdot\mathbf{x}} \tag{2.9}$$

Then, Equation (2.8) leads to the following ordinary differential equation which describes the behavior of the linear density perturbations.

$$\frac{\mathrm{d}^2\delta_{\mathbf{k}}}{\mathrm{d}t^2} + 2\frac{\dot{a}}{a}\frac{\mathrm{d}\delta_{\mathbf{k}}}{dt} = \left[4\pi G\bar{\rho}(t) - \frac{\sigma^2(t)k^2}{a^2}\right]\delta_{\mathbf{k}} \tag{2.10}$$

So, the density perturbations can grow only if the right-hand side of the Equation (2.10) stays positive; otherwise, the density perturbations will become oscillatory in nature, and structures will not form. This translates to satisfy the following condition.

$$\left[4\pi G\bar{\rho}(t) - \frac{\sigma^2(t)k^2}{a^2}\right] \geq 0 \tag{2.11}$$

This leads to the Jeans wave number and the physical Jeans scale as

$$k_{\mathrm{J}} = \left[\frac{4\pi G\bar{\rho}(t)a^2}{\sigma^2(t)k^2}\right]^{1/2} \implies \lambda_{\mathrm{J}}(t) = a\frac{2\pi}{k_{\mathrm{J}}} = \left[\frac{\pi\sigma^2(t)}{G\bar{\rho}(t)}\right]^{1/2}. \tag{2.12}$$

Jeans mass can then be scaled as

$$M_{\rm J}(t) = \frac{4\pi}{3}\rho_{\rm m}\left[\frac{\lambda_{\rm J}}{2}\right]^3 = \frac{4\pi}{3}\rho_{\rm m}\left[\frac{\pi\sigma^2(t)}{4G\bar{\rho}(t)}\right]^{3/2} . \tag{2.13}$$

Now, we can understand the evolution of the Jeans mass $M_{\rm J}(t)$ at different cosmic times following Equation (2.13).

- $t < t_{\rm NR}$: During the radiation dominated era, when the dark matter particles were relativistic in nature (i.e. $a < a_{\rm NR}$), $\sigma \sim c$, $\rho_{\rm m} \sim a^{-4}$ and $\bar{\rho} \sim a^{-4}$. This implies that the Jeans mass increases as $M_{\rm J} \sim a^2$.
- $t_{\rm NR} < t < t_{\rm MRE}$: Now, once the dark matter particles become non-relativistic in nature (i.e. $a_{\rm NR} < a < a_{\rm MRE}$), $\rho_{\rm m} \sim a^{-3}$ and $\sigma \sim a^{-1}$. So, during this period, the Jeans mass becomes constant $M_{\rm J} \sim$ const.
- $t > t_{\rm MRE}$: However, after the matter radiation equality, when the matter starts dominating over the radiation (i.e. $a > a_{\rm MRE}$), the background mean density evolves as $\bar{\rho} \sim a^{-3}$. Hence, the Jeans mass decreases substantially following $M_{\rm J} \sim a^{-3/2}$.

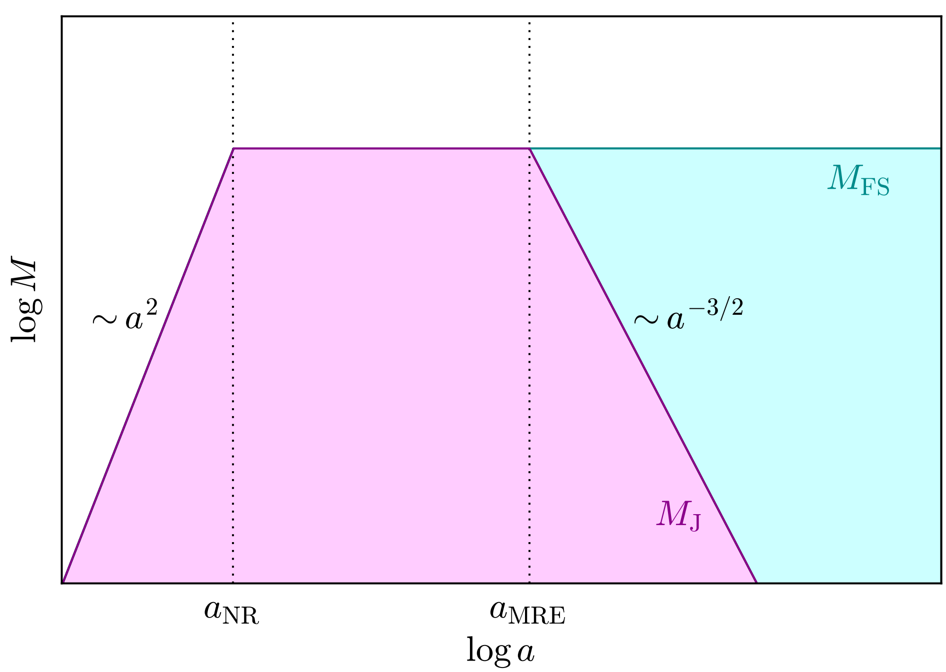


Figure 2.1: Schematic representation of the evolution of the Jeans mass (magenta line) and free streaming mass (cyan line) at different cosmic times.

Figure 2.1 shows how the Jeans mass evolves schematically. Density perturbations can not grow at a mass scale $M < M_{\rm J}$. So, the free streaming mass scale represents the maximum value that Jeans mass can have. Also, Schneider, Smith, and Reed (2013) have shown that at matter-radiation equality, the free streaming scale and Jeans scale happen to be of the same magnitude. In Figure 2.1, the magenta-colored region represents the mass scale of the density fluctuations with $M < M_{\rm J}$, and hence they can not grow while the cyan-colored region represents the mass scale of the density fluctuations with $M > M_{\rm J}$ and hence these perturbations can have the growing mode solution, but their initial perturbations are erased due to free streaming of the particles.

## 2.3 Simulating different dark matter cosmologies

It is not appropriate to follow the linear perturbation method (discussed in subsection 2.2.2) for the evolution of the dark matter field throughout the cosmic time, as it breaks down once $\delta > 1$. So, there are various numerical as well as analytical approaches that are widely used for simulating the evolution of the dark matter field.

In this work, we used a numerical approach for simulating the dark matter distribution. It is based on $N$ hypothetical dark matter particles which are moving in a force field defined by their self-gravity expressed as (where $1 < n < N$):

$$\mathbf{u}_n = \frac{d\mathbf{r}_n}{dt}; \qquad \mathbf{a}_n = \frac{d\mathbf{u}_n}{dt} = -\nabla\Phi(\mathbf{r}_n). \tag{2.14}$$

Then, we do the leap frog integration as follows.

1. We first calculate the particle positions at half a time step as

$$\mathbf{r}_n(t_{i+1/2}) = \mathbf{r}_n(t_i) + \mathbf{u}_n(t_i)\frac{\Delta t}{2}. \tag{2.15}$$

2. Then, we recalculate the forces using equation (2.14) for the particle positions at half a time step, and calculate the velocities of particles at a full time step as

$$\mathbf{u}_n(t_{i+1}) = \mathbf{u}_n(t_i) + \mathbf{a}_n(t_{i+1/2})\frac{\Delta t}{2}. \tag{2.16}$$

3. Finally, we drift the particle positions at a full time step as

$$\mathbf{r}_n(t_{i+1}) = \mathbf{r}_n(t_i) + [\mathbf{u}_n(t_i) + \mathbf{u}_n(t_{i+1})]\frac{\Delta t}{2}. \tag{2.17}$$

In the above leap frog integration scheme, the force calculation is computationally very expensive. For this purpose, there are various efficient approaches, including particle-particle algorithm, tree code, particle-mesh algorithm, particle-particle-particle-mesh algorithm (a combination of both tree and particle-mesh method), etc.

In this thesis, we used GADGET-2[1] N-body simulations (Springel 2005) for simulating the dark matter cosmologies. It is based on a particle-particle-particle mesh ($\mathrm{P^3M}$) method, which uses a tree algorithm for calculating the short-range forces and a particle mesh for long-range forces. Our simulations are done over a volume of $[50\ \mathrm{h^{-1}\ \ Mpc}]^3$ in comoving coordinates with $[1024]^3$ dark matter particles. The gravitational softening is chosen to be $1/30$ of the mean linear interparticle separation. The mass of each dark matter particle is $9.95 \times 10^6\ \mathrm{M_\odot}/h$, thereby dark matter haloes of $10^9\ \mathrm{M_\odot}/h$ are resolved with about 100 particles. Compared to other investigations of the dark matter structure formation, this is more focused on the small scales, and the volume and resolution used here are ideal for probing the EoR 21cm signal and the  induced effects.

The choice of the transfer function depends on how the dark matter particle is produced. Here, for the thermally produced dark matter, the initial conditions for  are generated according to the fitting formula presented in (Viel, Lesgourgues, et al. 2005), with thermal velocities drawn from a Fermi-Dirac distribution as

$$T^2_{\mathrm{WDM}}(k) = \frac{P^{\mathrm{lin}}_{\mathrm{WDM}}}{P^{\mathrm{lin}}_{\mathrm{CDM}}} = [1 + (\beta k)^{2\mu}]^{-10/\mu}, \tag{2.18}$$

where $\mu = 1.12$ and

$$\beta = 0.049 \left[\frac{\Omega_{\mathrm{WDM}}}{0.25}\right]^{0.11} \left[\frac{m_{\mathrm{WDM}}}{\mathrm{keV}}\right]^{-1.11} \left[\frac{h}{0.7}\right]^{1.22} h^{-1}\,\mathrm{Mpc}. \tag{2.19}$$

The characteristic scale at which the WDM power spectra have a cut off can be defined as the half mode scale $k_{\mathrm{hm}}$ where the transfer function

[1] https://wwwmpa.mpa-garching.mpg.de/gadget/

gets reduced to 1/2. From the choice of our transfer function given by Equation (2.18), we have

$$k_{\rm hm} = \frac{[(2)^{\mu/5} - 1]^{1/2\mu}}{\beta}. \tag{2.20}$$

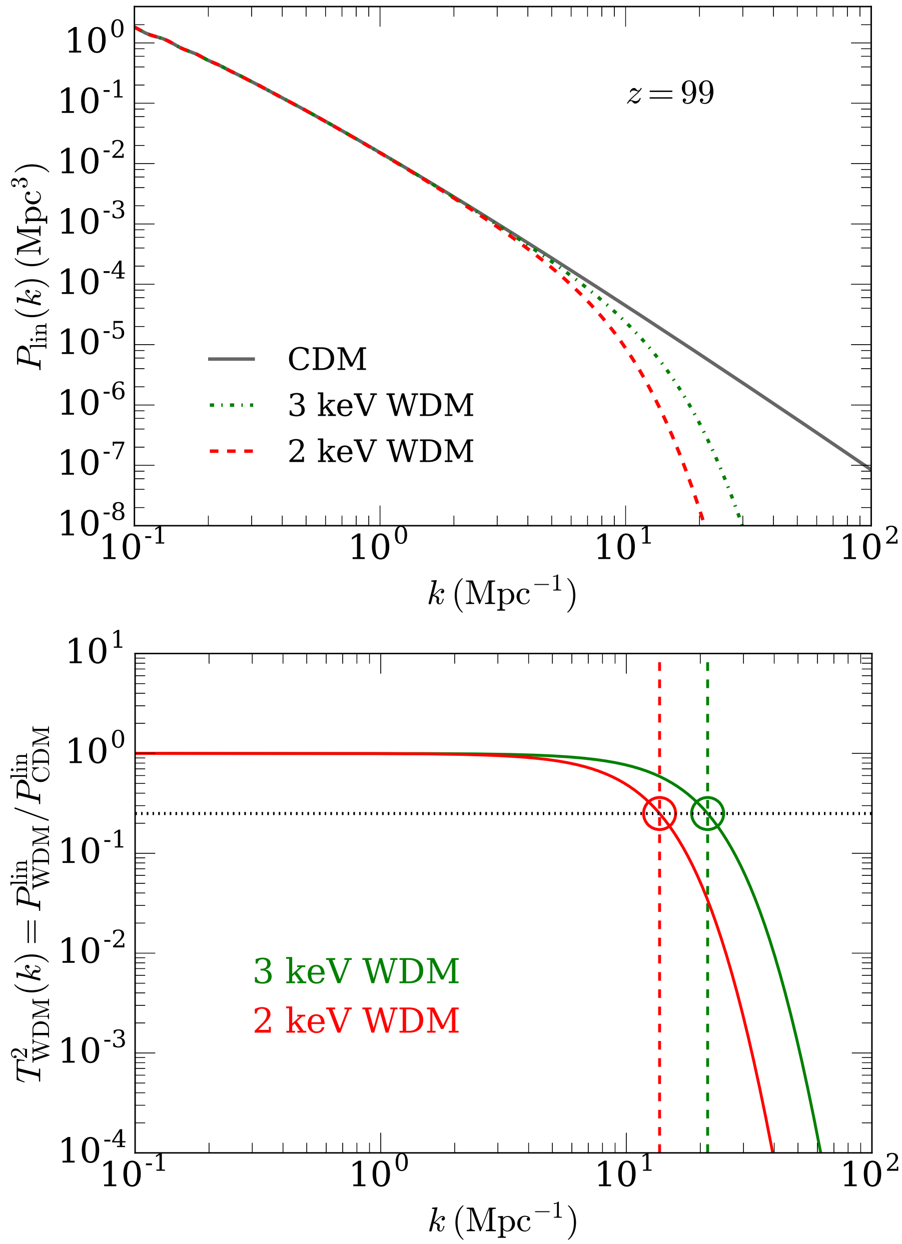


Figure 2.2: **Top panel:** Linear matter power spectra at $z = 99$ for CDM (solid grey), 3 keV WDM (dotted-dashed green) and 2 keV WDM (dashed red) model. **Bottom panel:** Squared transfer function along with the half-mode wavenumber for 3 keV WDM (green) and 2 keV WDM (red) model.

The top panel of Figure 2.2 shows the linear matter power spectra at $z = 99$ for CDM, 3 keV WDM and 2 keV WDM models. We notice that in WDM scenarios, the power gets suppressed on small scales (or large $k$ values). Also, as we decrease the value of $m_{\rm WDM}$, we see the damping of power at a larger length scale (or smaller $k$ mode). The bottom panel of Figure 2.2 shows the squared transfer function in WDM scenarios. The horizontal line represents the transfer function corresponding to the half-mode scale where $T_{\rm WDM}(k) = 1/2$. The vertical lines represent the wavenumber corresponding to the half-mode length scale $k_{\rm hm}$ in different dark matter models [see Equation 2.20]. They correspond to the length scale where the WDM first affects the halo properties.

The simulations' snapshots store the position and velocities of the dark matter particles at these predesignated redshifts. We, next use a Friends-of-Friend algorithm to identify the collapsed gravitationally bound objects (haloes) in these dark matter fields.

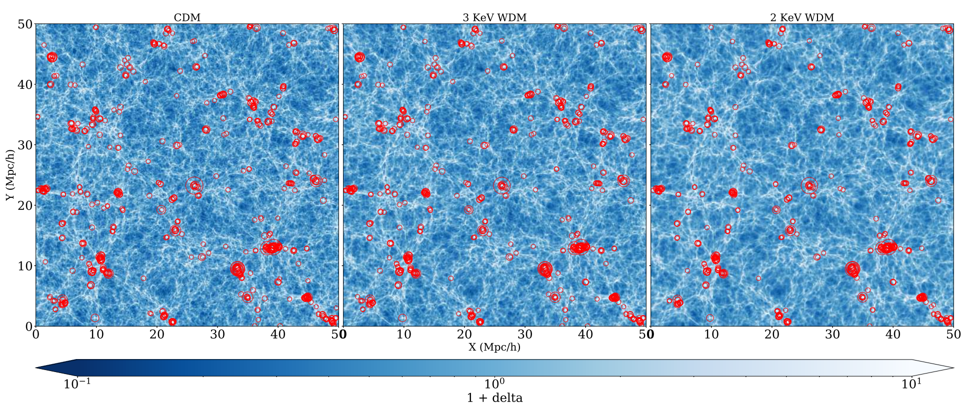


Figure 2.3: Dark matter overdensity field obtained from our simulation, over-plotted with the halo mass field at $z = 8$ using CIC algorithm for CDM (left panel), 3 keV WDM (central panel) and 2 keV WDM (right panel).

Figure 2.3 shows the two-dimensional slices of the matter overdensity field over-plotted with the halo fields obtained through these simulations. This plot shows all dark matter models at $z = 8$, where one can observe some visual evidence of the damping of matter density fluctuations on small scales in the WDM scenarios. Also, note that the free streaming length $\lambda_{\rm fs}$ scales with the mass of the warm dark matter particle as $\lambda_{\rm FS} \propto (m_{\rm WDM})^{-4/3}$.

These scaling relations have been derived in (Schneider, Smith, Macciò, et al. 2012; Smith et al. 2011). So, the lighter the WDM particle, the larger the free streaming scale, and the suppression will be more pronounced in 2 keV WDM model compared to 3 keV WDM model. This feature can also be seen in Figure 2.3 if we compare the matter overdensity and the halo mass field in the two WDM models.

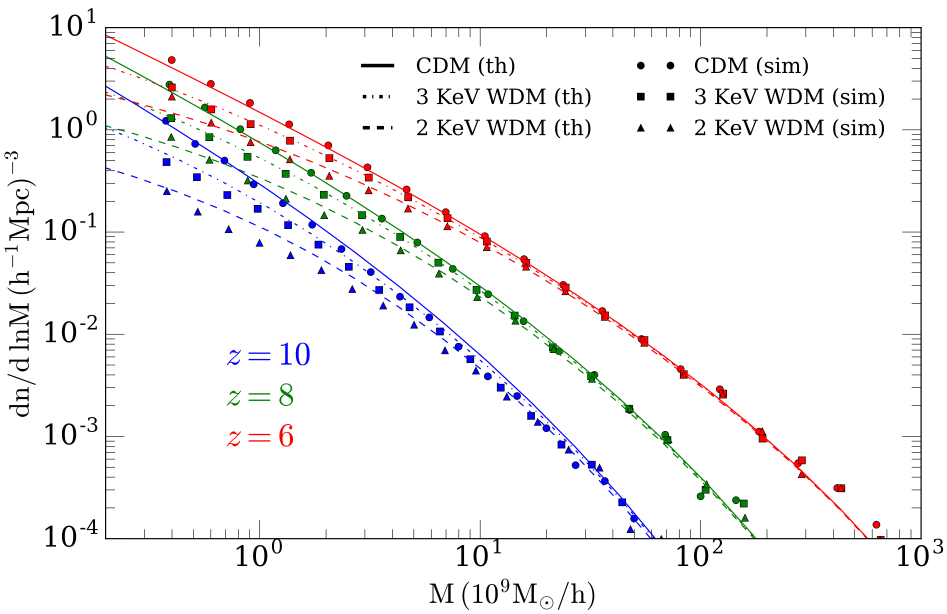


Figure 2.4: Halo mass function obtained through simulations for CDM (circles), 3 keV WDM (squares) and 2 keV WDM (triangles) model at z = 10 (blue), 8 (green) and 6 (red). The Sheth-Tormen mass function estimated using the top-hat window function is shown for CDM (solid), 3 keV WDM (dotted-dashed) and 2 keV WDM (dashed) model.

This suppression of density fluctuations at small scales will reduce the number of low mass halos in the WDM scenarios. In Figure 2.4, we show the halo mass function obtained at three redshifts $z$ = 10, 8, and 6 for all dark matter models. We observe that at any redshift, the number of low mass dark matter halos gets reduced in the WDM model if we compare it to the ΛCDM model. Also, we observe that the suppression of low mass halos is more for 2 keV WDM model compared to the 3 keV WDM model because the lighter the WDM particle, the larger the free streaming scale, and the formation of a more massive halo will be suppressed [see Equation (2.3)].

However, the number of massive halos in the WDM model is very similar to the CDM model, as, above the free streaming scale, the structure formation proceeds similarly to the CDM model. We have also shown the theoretically predicted Sheth-Tormen halo mass function estimated using a top-hat filter for all the dark matter models, where the transfer function in WDM scenarios is computed following the approach of Schneider, Smith, and Reed (2013); Viel, Lesgourgues, et al. (2005).

### 2.3.1 Effect of redshift space distortions on the density field

The peculiar velocities of the matter particles have a significant impact on the matter density field. It causes the overdense regions to get squeezed and underdense regions to get stretched along the line of sight. This effect, termed as redshift space distortions make any signal from this field, anisotropic in nature.

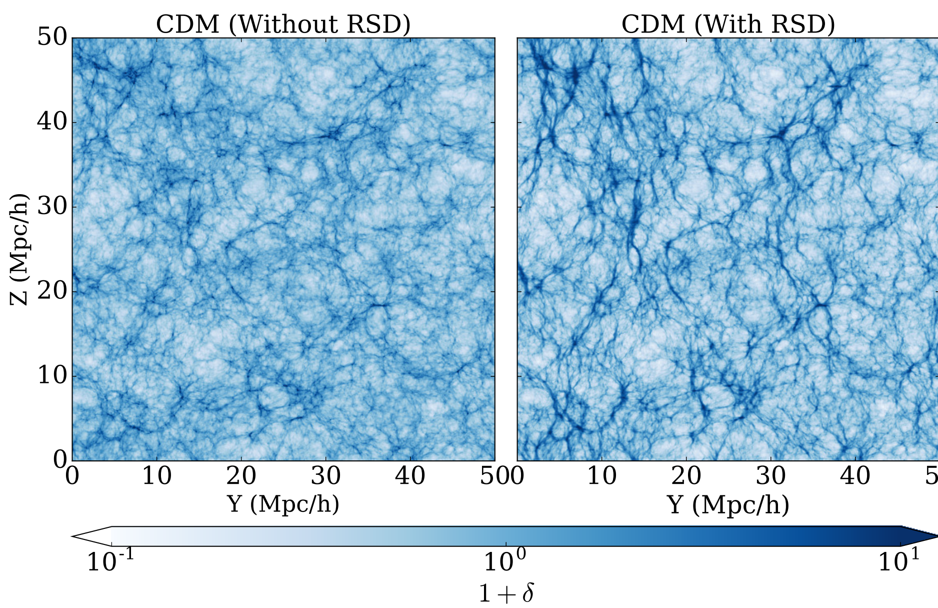


Figure 2.5: Effect of the redshift space distortions (RSD) on the overdensity field. Left panel: without RSD; Right panel: with RSD for CDM model. Here, we have chosen the $z$ direction as the line of sight.

To take into account its effect, we map the particle distribution from real space ($\mathbf{x}$) to redshift space ($\mathbf{s}$) using Equation (2.21).

$$\mathbf{s} = \mathbf{x} + \hat{n}\,\frac{\hat{n}\mathbf{v}_\mathrm{p}}{a\,H(a)}\,, \tag{2.21}$$

where $\hat{n}$ represents the line of sight from a distant observer and $\mathbf{v}_\mathrm{p} = \mathbf{v}/a$ is the peculiar velocity. So, the above mapping translates as

$$\mathbf{s} = \mathbf{x} + \hat{n}\,\frac{\hat{n}\mathbf{v}}{a^2 H(a)}\,. \tag{2.22}$$

Figure 2.5 shows the impact of redshift space distortions on the simulated overdensity field for CDM at $z = 8$. Here, we have chosen the $z$ direction as the line of sight, and one can notice that the redshift space distortions cause the over-densities to get squeezed and under-densities to get stretched along the $z$ direction.

## 2.4 Epoch of Reionization

About 400,000 years after the Big Bang at $z \sim 1100$, the cosmic expansion caused the Universe to get cooled enough so that the ions and electrons can combine to form neutral atoms. Immediately after the cosmological recombination, the photons decoupled from the matter and started to stream freely, which we observe today in the form of cosmic microwave background radiation, after which the Universe went into the dark ages. During the dark ages, the density fluctuations in the matter distribution, grew and the matter distribution collapsed at certain locations to make the first bound objects. These bound objects were the hosts for the first sources of light, the first stars and galaxies etc. These sources of light emitted the huge amount of ultraviolet and X-ray radiation, which gradually heated up and ionized the Universe (see Barkana et al. 2001; Fan et al. 2006; Furlanetto, Oh, et al. 2006, for reviews). This specific phase of the cosmic history when our universe had its last drastic phase change, from neutral to ionized, is known as the epoch of reionization.

However, some fundamental issues regarding this era, such as the exact redshift range that reionization spans, the nature of this process: sudden or gradual, homogeneous or inhomogeneous, and the sources responsible for the reionization (stars, quasars, exotic particles, etc.) are still unresolved. We discuss some of these in the next few subsections.

### 2.4.1 Reionization process

The gravitational instability in matter distribution initially drives the formation of galaxies in the high-density peaks of the matter density fluctuations.However, one also has to take into account all the baryonic physics to model the cooling of the gas and also the feedback effects within these galaxies (Dijkstra et al. 2006; Mo et al. 2010). The general understanding of galaxy formation tells us that the primordial gas first condenses in the potential wells created by dark matter, where it cools through the radiative processes and eventually fragments into the stars (Bromm and Larson 2004; Faucher-Giguère et al. 2010; Haiman et al. 2000). With the further condensation of the gas, the first stars and black holes begin to form. These objects work as sources of ionizing radiation. However, the efficiency of these objects to produce ionizing radiation depends on many complex astrophysical processes that goes on inside them.

The radiation emitted from these sources ionizes their immediate surroundings, and as a result, ionized H II bubbles form around these sources. These bubbles grow in size as the photons traverse through the IGM. With time, as more ionizing sources form, the number and size of these bubbles increase, and eventually, the Universe gets ionized.

However, one has to quantify how many of these ionizing photons can escape from the galactic environment into the IGM and ionize it i.e. escape fraction of the ionizing photons. It is difficult to constrain this parameter observationally due to the lack of information at high redshifts (B. Ciardi et al. 2002; Rivera-Thorsen et al. 2019; Steidel et al. 2001). Also, we do not know what decides the formation of these sources of light and the number of ionizing photons that they emit. One has to understand all the baryonic physics, galaxy formation and evolution, and properties of metal-poor stars to answer these questions.

### 2.4.2 Sources of Reionization

We need ultraviolet photons to ionize the Universe as the ionization energy of a hydrogen atom is 13.6 eV. The sources of these UV photons include the first stars (Population III stars), second-generation stars (Population II stars), and mini quasars. Population III stars were formed out of the primordial gas clouds, which only contain hydrogen and helium. To form a star, the gas cloud has to find a cooling mechanism so that it can radiate some energy, which is gained by gravitational contraction. Population III stars are very different from the present-day stars as they do not contain the dust grains and molecules with heavy elements, and this makes them a poor radiator of energy. As a result, the star-forming clumps for these stars reach high temperatures and they become very massive. This type of stars can efficiently produce UV photons, but their lifetime is generally short (see Ishiyama et al. 2016; Yoshida, Bromm, et al. 2004, for reviews). At the end of their life, some of these stars would have exploded as supernovae and expelled the metals generated in their cores into the IGM, whereas some of them would have also ended up in a black hole (Madau et al. 2001).

The transition from Population III to Population II stars occur due through this process of metal enrichment. Population II stars can cool efficiently due to the metal enrichment, and so they were less massive. The gas clouds, of which these Population II stars form, have a metallicity $Z \geq 10^{-4}\ Z_{\odot}$ (Barkana et al. 2001; Benedetta Ciardi et al. 2005).

Quasars have also been considered as the source of ionizing radiation. They are the black hole powered sources that emit X-ray photons, and these photons can heat the IGM much further from the source than the UV photons, due to their longer mean free path. The ionization profile around these mini-quasars is similar to that of the stars, but the heating profile is generally very different as the X-ray photons can penetrate through the IGM, and even after absorption, their energy is sufficient to heat the medium (Thomas et al. 2008).

Although stars have been considered as the primary source in most of the reionization studies (Bromm, Coppi, et al. 2002; Yoshida, Abel, et al. 2003), several studies have focused on mini-quasars as an essential contributor (Furlanetto and Loeb 2002; Furlanetto, Zaldarriaga, et al. 2004; Ricotti et al. 2004). Though there is considerable uncertainty about the ionizing sources, the observational data up to $z \sim 6$ suggests that the ionizing source population can potentially be a mixture of stars and mini-quasars.

Observationally, we can probe this period by several indirect methods. The two widely used methods among these are

1. the absorption spectra of high redshift quasars, but it is not a useful probe at $z \sim 6$ because the absorption lines become saturated at these redshifts (Loeb et al. 2001; White et al. 2003) and,

2. the optical depth due to Thompson scattering for the CMBR but it can only constrain the integrated reionization history (Kaplinghat et al. 2003; Komatsu et al. 2011).

The 21-cm line, which arises due to the hyperfine splitting of the ground state in a neutral hydrogen atom, is a crucial and direct probe to study this period. In the next section, we discuss how it can be used as an observational probe.

## 2.5 Observing the structures in the early Universe: 21-cm signal

21-cm signal, which arises due to the hyperfine splitting in the ground state of neutral hydrogen atom because of the interaction between the proton and electron magnetic moment is a key direct probe of the EoR. The $1s$ ground state of hydrogen splits into two distinct energy levels, namely $1s$-singlet and $1s$-triplet states, which are separated by a wavelength of 21.1 cm (or a frequency of 1420.4 MHz). This signal is characterized using the spin temperature, which is the excitation temperature of the signal. It quantifies the ratio of the number density of hydrogen atoms in the triplet and the singlet state.

$$\frac{n_1}{n_0} = \frac{g_1}{g_0} \exp\left(\frac{-T_*}{T_S}\right), \tag{2.23}$$

where $n_1$ and $n_0$ are the number densities of hydrogen atoms in the triplet and singlet state respectively, $g_1/g_0$ shows the ratio of degeneracy factors ($g_1/g_0 = 3$), $T_* = h\nu_e/k_B = 0.068\,\mathrm{K}$ ($\nu_e = 1420.4$ MHz) and $T_S$ is the spin temperature.

Three processes that decides the spin temperature $T_S$ and so the ratio $n_1/n_0$ are: (i) Radiative transition due to the interaction of 21-cm photons with the CMB, (ii) Collisional transition due to the collision of the photons with the hydrogen atoms or electrons (Furlanetto, Oh, et al. 2006) and (iii) Lyman-$\alpha$ pumping which results in the spin-flip via an intermediate state (Pritchard et al. 2006; Wouthuysen 1952). In equilibrium, the spin temperature will get coupled to the CMB temperature $T_\gamma$, the kinetic temperature of the gas $T_{\mathrm{K}}$, and color temperature $T_{\mathrm{K}}$ (where $T_{\mathrm{C}} \approx T_{\mathrm{K}}$) for the three processes respectively. The rate equation which decides the dynamics of $n_1/n_0$ can be written as:

$$\dot{n}_0 = -n_0 \left(P_{01}^{\gamma} + P_{01}^{C} + P_{01}^{\alpha}\right) + n_1 \left(P_{10}^{\gamma} + P_{10}^{C} + P_{10}^{\alpha}\right), \tag{2.24}$$

where $P_{01}^{\gamma}$, $P_{01}^{C}$ and $P_{01}^{\alpha}$ are the excitation rates and $P_{10}^{\gamma}$, $P_{10}^{C}$ and $P_{10}^{\alpha}$ are the de-excitation rates due to radiative transition, collisional transition and lyman-$\alpha$ pumping respectively.

From the argument of detailed balance where each process is balanced individually in equilibrium, one arrives at:

$$T_{\mathrm{S}}^{-1} = \frac{T_\gamma^{-1} + x_{\mathrm{c}} T_{\mathrm{K}}^{-1} + x_\alpha T_{\mathrm{C}}^{-1}}{1 + x_{\mathrm{c}} + x_\alpha}, \tag{2.25}$$

where $x_{\mathrm{c}} = P_{10}^{C}/P_{10}^{\gamma}$ and $x_\alpha = P_{10}^{\alpha}/\,P_{10}^{\gamma}$ are the efficiencies of collisional coupling and lyman-$\alpha$ coupling respectively.

By solving the radiative transfer equation for the CMB photons traveling through the hydrogen clouds, one can arrive at the following expression for the 21-cm brightness temperature as:

$$\begin{aligned}\delta T_{\mathrm{b}} = 27\, x_{\mathrm{H\,I}}(1+\delta_{\mathrm{b}}) \left(\frac{\Omega_{\mathrm{b}} h^2}{0.023}\right) \left(\frac{0.15}{\Omega_{\mathrm{m}} h^2} \frac{1+z}{10}\right)^{1/2} \\ \times \left(\frac{T_{\mathrm{S}} - T_\gamma}{T_{\mathrm{S}}}\right) \left[\frac{\partial_{\mathrm{r}} v_{\mathrm{r}}}{(1+z)H(z)}\right],\end{aligned} \tag{2.26}$$

where $x_{\mathrm{H\,I}}$ is the neutral hydrogen fraction, $\delta_{\mathrm{b}}$ is the fractional baryon overdensity, $T_{\mathrm{S}}$ and $T_\gamma$ are the spin temperature and the CMB temperature respectively, and the last term accounts for the velocity gradient along the line of sight.

# Chapter 3

# Simulating the redshifted EoR 21-cm signal

We have used the ReionYuga[1] semi-numerical simulations to simulate the redshifted 21-cm signal (Majumdar, Bharadwaj, et al. 2013; Majumdar, Mellema, et al. 2014; Mondal et al. 2017). This simulation method is somewhat similar to the methods followed by Choudhury et al. (2009); Furlanetto, Zaldarriaga, et al. (2004); Mesinger et al. (2011); Zahn et al. (2011). Steps that are involved in this method can be summarized as follows: (I) Generating the dark matter density field, (II) Identifying the position and mass of the collapsed structures, i.e. haloes, in the dark matter field, (III) Assigning the ionizing photon production rates to these haloes, (IV) Generating the ionization maps including the effect of redshift space distortions and (V) Converting these ionization maps into redshifted 21-cm brightness temperature field.

As discussed in section 2.3, we have used GADGET 2.0 N-body simulations to accomplish steps I and II. For the purpose of this work, we next assumed that the hydrogen follows the simulated dark matter distribution at these redshifts (Table 3.1). Further, as our reionization source model (step III), we assume that the number of ionizing photons produced by a halo is proportional to its mass (Choudhury et al. 2009; Majumdar,

[1] https://github.com/rajeshmondal18/ReionYuga

Mellema, et al. 2014):

$$N_\gamma(M) = N_{\rm ion}\frac{M}{m_{\rm H}}\,, \tag{3.1}$$

where $m_{\rm H}$ is the mass of a hydrogen atom, $M$ is the mass of the halo, and $N_{\rm ion}$ is a dimensionless free parameter, which may depend on various other degenerate reionization parameters including star-formation efficiency of a source, escape fraction of ionizing photons from these sources, etc. We set $N_{\rm ion} = 23.21$ to achieve $\bar{x}_{\rm H\,I} \approx 0.5$ at $z = 8$ in the ΛCDM model. This additionally ensures that for the ΛCDM scenario, reionization ends by $z \sim 6$ and produces a Thompson scattering optical depth that is consistent with the CMBR observations.

Table 3.1: This tabulates the redshift $z$ and corresponding mass averaged neutral fraction $\bar{x}_{\rm H\,I}$ for all the dark matter models, for which we have simulated the 21-cm signal.

| Redshift $z$ | $\bar{x}_{\rm H\,I}$ (CDM) | $\bar{x}_{\rm H\,I}$ (3 keV WDM) | $\bar{x}_{\rm H\,I}$ (2 keV WDM) |
|---|---|---|---|
| 10.00 | 0.84 | 0.90 | 0.94 |
| 9.25 | 0.75 | 0.84 | 0.90 |
| 9.00 | 0.71 | 0.81 | 0.88 |
| 8.65 | 0.64 | 0.77 | 0.84 |
| 8.00 | 0.47 | 0.64 | 0.75 |
| 7.50 | 0.30 | 0.51 | 0.64 |
| 7.00 | 0.11 | 0.34 | 0.51 |
| 6.00 | 0.00 | 0.03 | 0.13 |

Next we perform the step IV, i.e. we produce the ionization map, using the H I density map and the ionizing photon density maps. We use an excursion-set based algorithm to produce the ionization map at the desired redshifts. In this formalism, we first map the hydrogen density and ionizing photon density fields on a coarser $[1024/8]^3 = [128]^3$ grid with grid spacing $[0.07 \times 8] = 0.56$ Mpc. Next, to identify the ionized regions, we smooth both the H I and ionizing photon fields using spheres of radius $R$ for $R_{\rm min} \leq R \leq R_{\rm max}$, where $R_{\rm min}$ is the resolution of the simulation which is equal to the grid spacing and $R_{\max}$ is the mean free path of the ionizing photon ($R_{\rm mfp}$). In these simulations, we keep the value of the mean free path of the ionizing photons $R_{\rm mfp} = 20$ Mpc. The choice of the value of $R_{\rm mfp}$ is inspired by the findings of Songaila et al. (2010). For any grid point $\mathbf{x}$, if the averaged ionizing photon density $\langle n_\gamma(\mathbf{x})\rangle_{\rm R}$ exceeds the averaged H I density $\langle n_{\rm H}(\mathbf{x})\rangle_{\rm R}$ for any $R$, then we flag that grid point to be ionized. The points which do not meet this criteria, we assign an ionization fraction $x_{\rm H\,II}(\mathbf{x}) = \langle n_\gamma(\mathbf{x})\rangle_{\rm R_{min}}/\langle n_{\rm H}(\mathbf{x})\rangle_{\rm R_{min}}$ to them. This is repeated for all grid points in the simulation volume and for all $R$ within the allowed range and the ionization map is produced. This ionization is then converted into the 21-cm H I brightness temperature map (step V) following the Equation (3.2).

$$\begin{aligned}\delta T_{\rm b} = 27\, x_{\rm H\,I}\,(1+\delta_{\rm b})\left(\frac{\Omega_{\rm b}\, h^2}{0.023}\right)\left(\frac{0.15}{\Omega_{\rm m}\, h^2}\frac{1+z}{10}\right)^{1/2} \\ \times\left(\frac{T_{\rm s}-T_\gamma}{T_{\rm s}}\right),\end{aligned} \tag{3.2}$$

where $x_{\rm H\,I}$ is the neutral hydrogen fraction, $\delta_{\rm b}$ is the fractional baryon overdensity, $T_{\rm s}$ and $T_\gamma$ are the spin temperature and the CMB temperature respectively. In this work, we assume that during reionization the IGM is substantially heated above the CMB ($T_{\rm s} \approx T_{\rm K} \gg T_\gamma$). This is a reasonable assumption once the global neutral fraction is $x_{\rm H\,I} \leq 0.9$ and has been independently observed in different studies of reionization (Choudhury et al. 2009; Furlanetto, Zaldarriaga, et al. 2004; Majumdar, Bharadwaj, et al. 2013; Majumdar, Mellema, et al. 2014; Mondal et al. 2017). So, the term $(T_{\rm s} - T_\gamma)/T_{\rm s} \to 1$ in Equation (3.2). The matter peculiar velocities will make the redshifted 21-cm signal anisotropic along the line-of-sight of a present day observer. This unavoidable anisotropy in any cosmic signal is popularly known as the redshift space distortions (see Figure 2.5). We follow the formalism of Majumdar, Bharadwaj, et al. (2013) to map the real space brightness temperature field into the redshift space.

## 3.1 One-point statistics of the simulated EoR 21-cm signal

Once the redshift space 21-cm H I brightness temperature maps are produced, we estimate the one-point statistics (e.g. variance, skewness, etc.) of this signal. For a continuous random variable $x$, following the probability density function $f(x)$ with the mean $\bar{x}$, the variance and the skewness can be calculated following equation (3.3) and (3.4) as

$$\sigma^2 = \int_{-\infty}^{\infty} (x-\bar{x})^3 f(x)\mathrm{d}x \tag{3.3}$$

$$\gamma_1 = \frac{\mu_3}{(\sigma^2)^{3/2}} = \frac{\int_{-\infty}^{\infty} (x-\bar{x})^3 f(x)\mathrm{d}x}{\left(\int_{-\infty}^{\infty} (x-\bar{x})^2 f(x)\mathrm{d}x\right)^{3/2}} . \tag{3.4}$$

However, we will estimate these statistics in the distribution of brightness temperature $T_\mathrm{b}(\mathbf{x})$ simulated at $(128)^3$ grid, which is a discrete distribution. In this case, equations (3.3) and (3.4) translates to

$$\sigma^2 = \frac{1}{N}\sum_i \left(T_i - \bar{T}\right)^2 \tag{3.5}$$

$$\gamma_1 = \frac{\frac{1}{N}\sum_i \left(T_i - \bar{T}\right)^3}{\left[\frac{1}{N}\sum_i \left(T_i - \bar{T}\right)^2\right]^{3/2}} , \tag{3.6}$$

where $N = (128)^3$ is the total number of pixels (or grid points) in the simulation volume, $T_i$ is the brightness temperature at the $i^{th}$ pixel, and $\bar{T}$ is the mean brightness temperature.

## 3.2 Fourier Statistics of the simulated EoR 21-cm signal

Visibilities, which are the Fourier transform of the sky brightness temperature, are the basic observables in any radio interferometric observation. This is one of the major reasons why most of the efforts to quantify the 21-cm signal are focused on using various Fourier statistics. For this work, we consider an idealistic scenario where there is no foreground emission or noise present in the data, and the visibilities contain only the Fourier transform of the signal brightness temperature $\Delta T_\mathrm{b}(\mathbf{k})$. The two Fourier statistics that are in our focus for this work are the power spectrum and bispectrum.

### 3.2.1 21-cm power spectrum

One can define the 21-cm power spectrum as

$$\langle \Delta T_\mathrm{b}(\mathbf{k})\Delta T_\mathrm{b}(\mathbf{k}')\rangle = (2\pi)^3\delta^3(\mathbf{k}-\mathbf{k}')P(k) , \tag{3.7}$$

where $\delta^3(\mathbf{k}-\mathbf{k}^{'})$ is the Dirac delta function, defined as

$$\delta^3(\mathbf{k}-\mathbf{k}^{'}) = \begin{cases} 1, & \text{if } \mathbf{k}=\mathbf{k}^{'} \\ 0, & \text{otherwise}\,. \end{cases} \tag{3.8}$$

To estimate the 21-cm power spectrum, we divide the entire $k$ range (determined by the smallest and largest length scales probed by our simulation) into 10 equispaced logarithmic bins. Next, we Fourier transform the simulated 21-cm brightness temperature volume and use Equation (3.7) to estimate the power spectrum.

### 3.2.2 21-cm bispectrum

Similar to the power spectrum the bispectrum can be defined as

$$\langle \Delta T_{\rm b}(\mathbf{k_1})\Delta T_{\rm b}(\mathbf{k_2})\Delta T_{\rm b}(\mathbf{k_3})\rangle = V\delta^3_{\mathbf{k_1}+\mathbf{k_2}+\mathbf{k_3},\,0} B_{\rm b}(\mathbf{k_1},\mathbf{k_2},\mathbf{k_3})\,, \tag{3.9}$$

where $\delta^3_{\mathbf{k_1}+\mathbf{k_2}+\mathbf{k_3},\,0}$ is the Kronecker Delta function that ensures that the three $\mathbf{k}$-modes involved form a closed triangle (see top panel of Figure 3.1) i.e.

$$\delta^3_{\mathbf{k_1}+\mathbf{k_2}+\mathbf{k_3},0} = \begin{cases} 1, & \text{if } (\mathbf{k_1}+\mathbf{k_2}+\mathbf{k_3}) = 0 \\ 0, & \text{otherwise}\,. \end{cases} \tag{3.10}$$

Following the definition of the bispectrum one can define a binned estimator for this statistic as

$$\hat{B}(\mathbf{k_1},\mathbf{k_2},\mathbf{k_3}) = \frac{1}{NV} \sum_{(\mathbf{k_1}+\mathbf{k_2}+\mathbf{k_3}=0)\in n} \Delta T_{\rm b}(\mathbf{k_1})\Delta T_{\rm b}(\mathbf{k_2})\Delta T_{\rm b}(\mathbf{k_3})\,, \tag{3.11}$$

where the total number of triangles that belong to the $n^{th}$ triangle configuration bin is $N$, and $V$ is the simulation volume. To estimate the bispectra from the simulated signal we follow the algorithm of Majumdar, Pritchard, et al. (2018). In their algorithm Majumdar, Pritchard, et al. (2018) have parametrized the triangle configurations using two independent parameters:

1. The ratio between the length of the two arms of a $\mathbf{k}$ triangle

$$k_2/k_1 = n. \tag{3.12}$$

2. The cosine of the angle between these two arms

$$\cos\theta = \frac{\mathbf{k_1}\cdot\mathbf{k_2}}{k_1 k_2}\,. \tag{3.13}$$

This parametrization helps in reducing the overall computation time for bispectrum estimation.

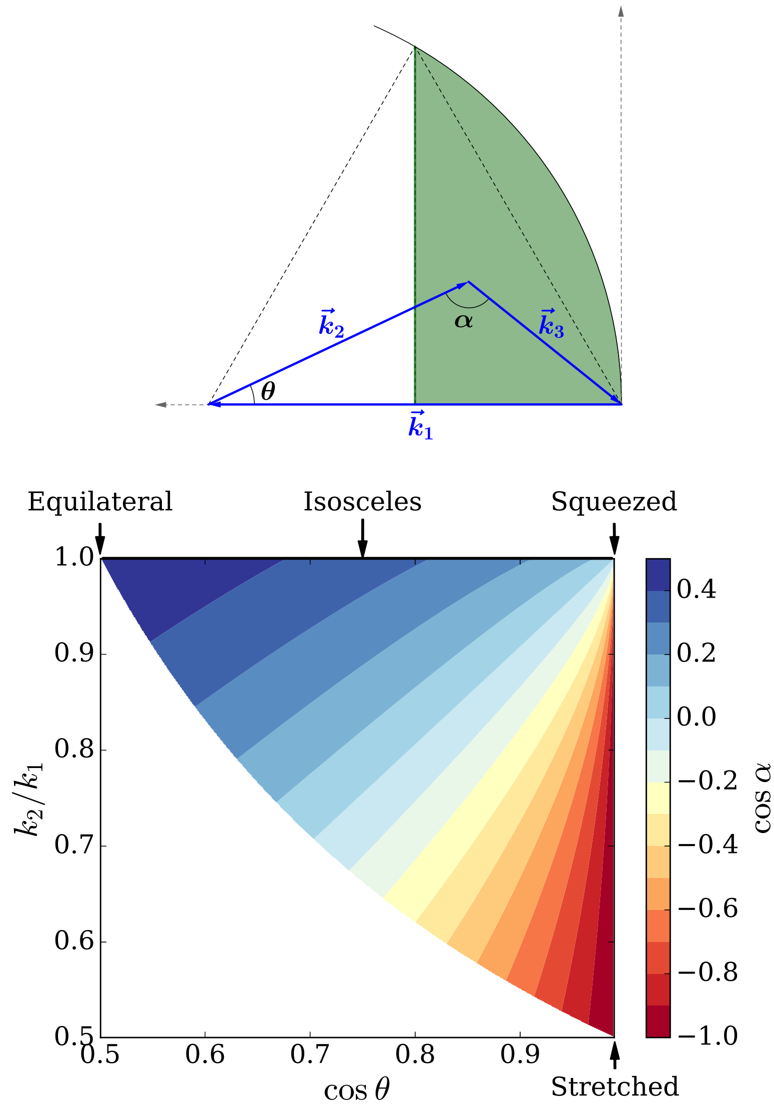


Figure 3.1: **Top panel:** For our unique triangle configurations, the tip of the $\mathbf{k_2}$ can move only in the green shaded region shown here, thereby satisfying Equation 3.14. **Bottom panel:** Unique triangles parameter space in terms of $\cos\alpha$ showing the different limits of the $k$-triangles (Bharadwaj, Mazumdar, et al. 2020), for which we estimate the bispectra

For a comprehensive understanding of the 21-cm bispectra, we need to estimate the bispectrum for all possible unique triangle configurations. We follow the prescription of Bharadwaj, Mazumdar, et al. (2020), that allows us to identify all possible unique triangles using the two parameters defined in Equations (3.12) and (3.13) and by imposing the additional condition on the triangle parameter space i.e.

$$k_1 \geq k_2 \geq k_3 \implies \frac{k_2}{k_1} \cos\theta \geq 0.5. \tag{3.14}$$

Figure 3.1 shows the unique triangle configurations in the $n - \cos\theta$ parameter space.

# Chapter 4

# Results and Discussion

## 4.1 Reionization history and 21-cm topology

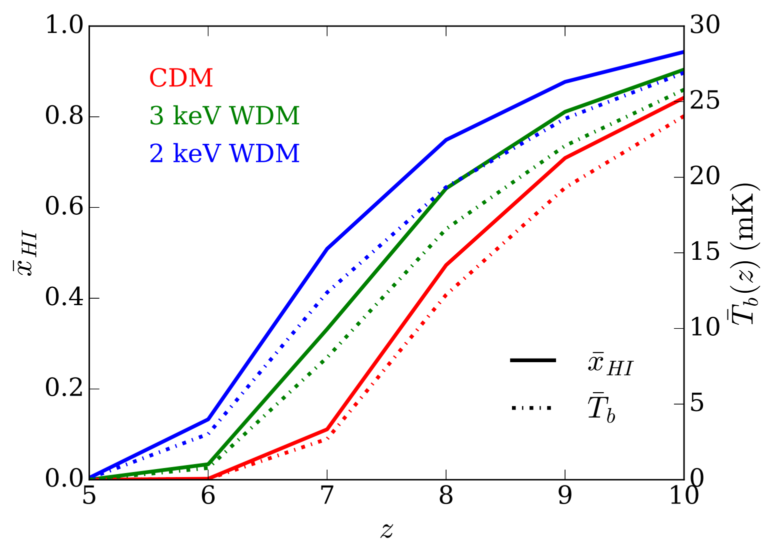


Figure 4.1: Reionization history for CDM (red), 3 keV WDM (green) and 2 keV WDM (blue) with the variation of mass avg. neutral fraction $\bar{x}_{\mathrm{H\,I}}$ (solid) and mean 21-cm brightness temperature $\bar{T}_{\mathrm{b}}$ (dotted-dashed) with redshift $z$

The differences in the dark matter models have two prominent impact on the 21-cm signal from the EoR. One of them is the delay in the global reionization process, which is evident from the $\bar{x}_{\mathrm{H\,I}} - z$ and $\bar{T}_{\mathrm{b}} - z$ curves for different dark matter models in Figure 4.1. The reionization starts and finishes later in the WDM scenarios compared to the CDM scenario. This is a clear signature of the differences in the structure formation history in different scenarios (shown through the halo mass functions in Figure 2.4). The halo mass functions plotted in Figure 2.4 reveals that the low mass halos cumulatively are the dominant sources of ionizing photons (when we assume all halos are equally efficient in producing ionizing photons) at any redshift for all dark matter models considered here. In case of the warm dark matter models, the low mass end of the halo mass function gets suppressed compared to the cold dark matter scenario, which results in an overall decrease in the total number of ionizing photons produced at any redshift. This overall reduction in the total number of ionizing photon produced at any redshift leads to a delay in the reionization process for the WDM models compared to the CDM one. The suppression of the low mass end of the halo mass function is more pronounced in the case of the 2 keV WDM model compared to the 3 keV WDM model, which leads to an even longer delay in the reionization process in case of the 2 keV WDM model.

The other prominent impact that the differences in the dark matter models on the reionization process have is the differences in the H I 21-cm brightness temperature topology. This is also caused by the different level of suppression of the low mass end of the halo mass function in different dark matter models. Figure 4.2 shows two-dimensional slices of the H I 21-cm brightness temperature maps at three different redshifts: $z = 9$, 8 and 7 for all dark matter models. In these figures, a clear difference in the size and location of the ionized regions is visible in different models of dark matter. However, it is important to note that even if the 21-cm maps are shown at the same redshifts, they are not at the same state of reionization for different models of the dark matter. One may ask the question how much of this observed difference in 21-cm topology is due to the delay in reionization history. To address this, Das et al. (2018) have tuned the ionizing photon production efficiency (i.e. the parameter $N_{\rm ion}$ in our simulations) of halos in different dark matter models to get the same global neutral fraction at the same redshifts for all dark matter models. With this modification in their simulations, they still observed significant differences in the 21-cm topology and its Fourier statistics for different dark matter scenarios. However, one should note that, changing the $N_{\rm ion}$ in different scenarios effectively means changing the reionization model all together. Therefore, for the main analysis and results in this paper we keep the value of $N_{\rm ion}$ same for all dark matter scenarios. We briefly discuss the impact of changing the $N_{\rm ion}$ (to get the same reionization history) for different dark matter models on the 21-cm statistics (observable) in section 4.4.

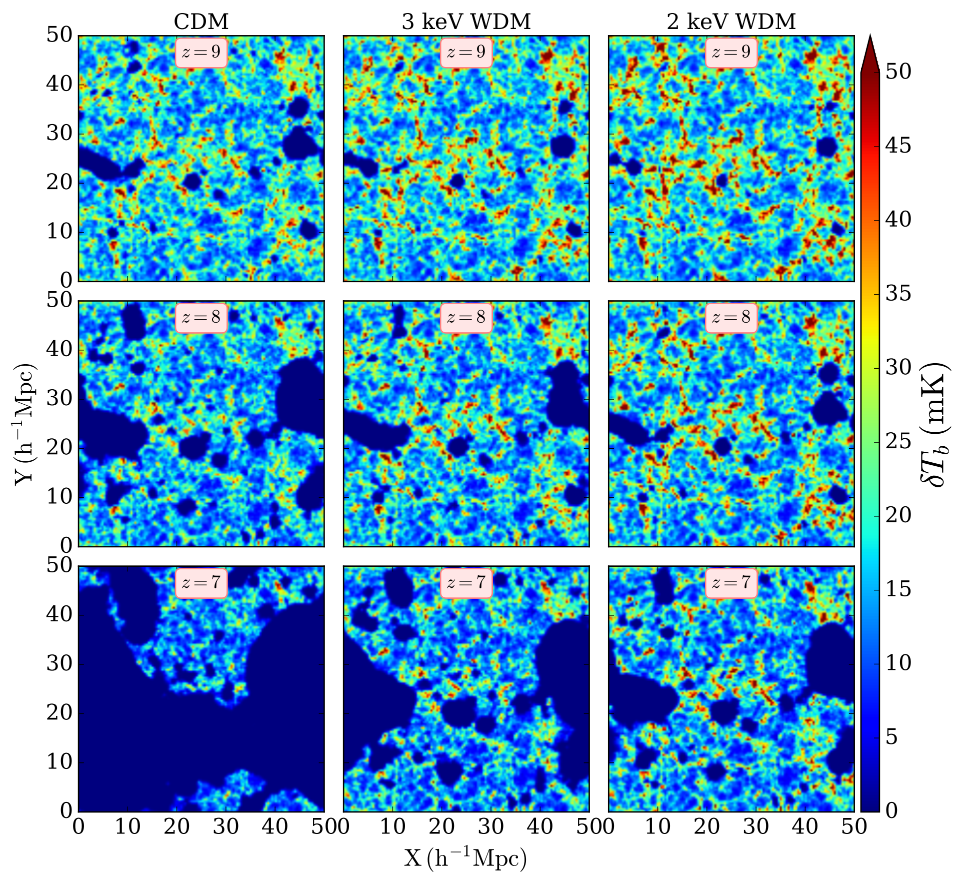


Figure 4.2: The three columns show the redshift space 21-cm H I brightness temperature maps for CDM, 3 keV WDM and 2 keV WDM (from left to right) respectively at $z$ = 9, 8 and 7 (from top to bottom). The color-bar represents the amplitude of 21-cm brightness temperature.

## 4.2 One-point statistics of the signal

To begin with, we first focus our attention to the one-point statistics of the 21-cm signal: variance and skewness. We estimate these statistics based on the distribution of 21-cm brightness temperature $\delta T_{\rm b}(\mathbf{x})$.

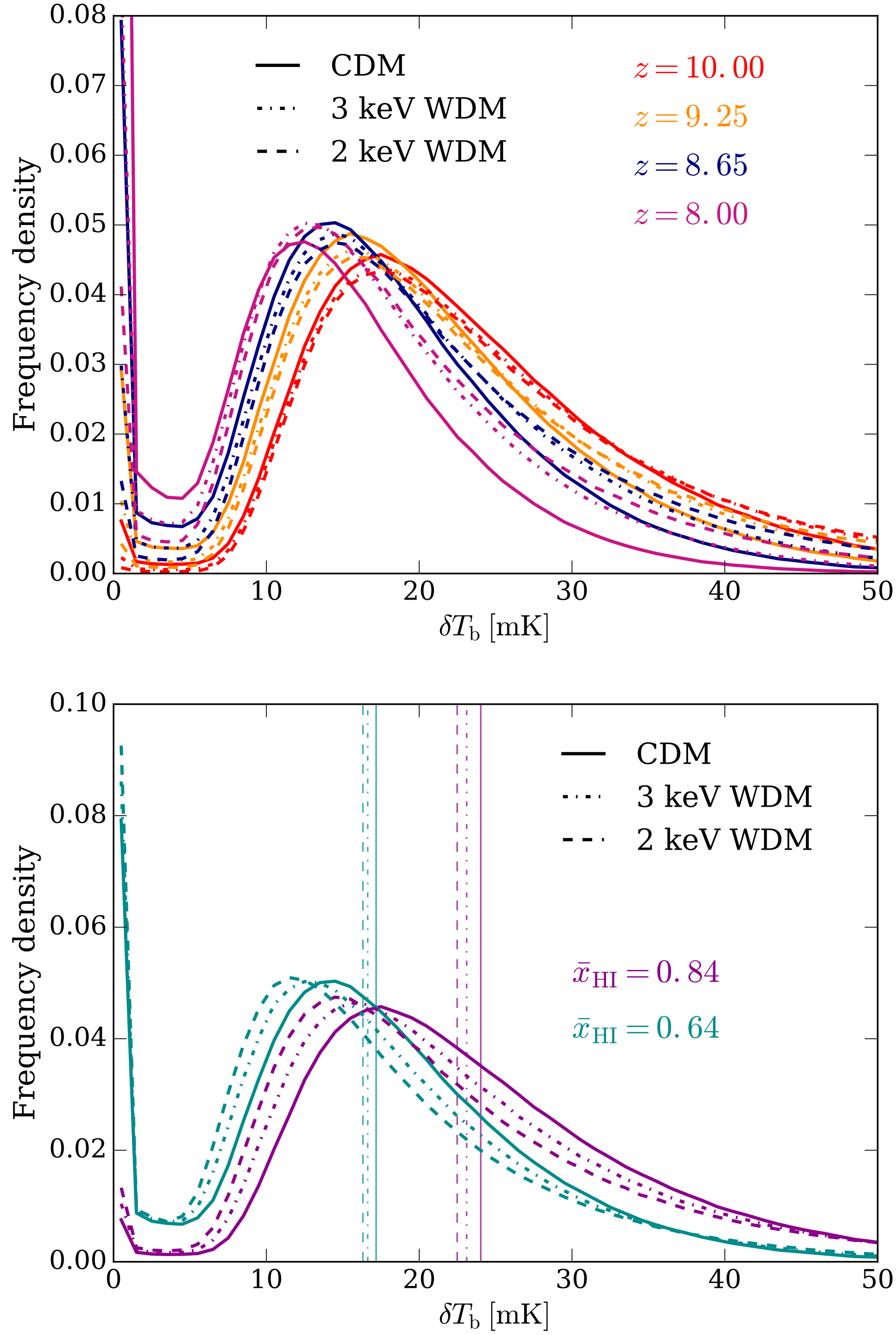


Figure 4.3: Distribution of 21-cm brightness temperature $\delta T_{\mathrm{b}}(\mathbf{x})$ for CDM (solid), 3 keV WDM (dotted-dashed) and 2 keV WDM (dashed) compared at same redshift (top panel), and at the same neutral fraction (bottom panel). The vertical line represents the mean $\bar{T}_{\mathrm{b}}$ at these neutral fraction values.

The top panel of Figure 4.3 shows the probability density function (PDF) of the simulated $\delta T_{\rm b}(\mathbf{x})$ at different redshift for all the models. One can also notice the signature of an inside-out topology of reionization in all the dark matter models. This moves the high brightness temperature points [or equivalently high density regions; $\delta T_{\rm b} \propto (1+\delta)$] into the $\delta T_{\rm b} = 0$ bin (where $x_{\rm H\,I} = 0$) as the reionization progresses with decreasing redshift.

### 4.2.1 Variance

Figure 4.4 shows the evolution of $\delta T_{\rm b}$ variance as a function of redshift. From the figure, we observe that the variance decreases as the reionization progresses (with decreasing $z$) for any DM model. This is because with the progressing state of reionization, the spread in the distribution of $\delta T_{\rm b}$ also decreases as the high $\delta T_{\rm b}$ tail gets shorten (see Figure 4.3).

Further, in Table 4.1, we compare the variance at the same neutral fraction and observe that at any stage of reionization, the variance varies with the DM model as: $\sigma^2$ (CDM) < $\sigma^2$ (3 keV WDM) < $\sigma^2$ (2 keV WDM).

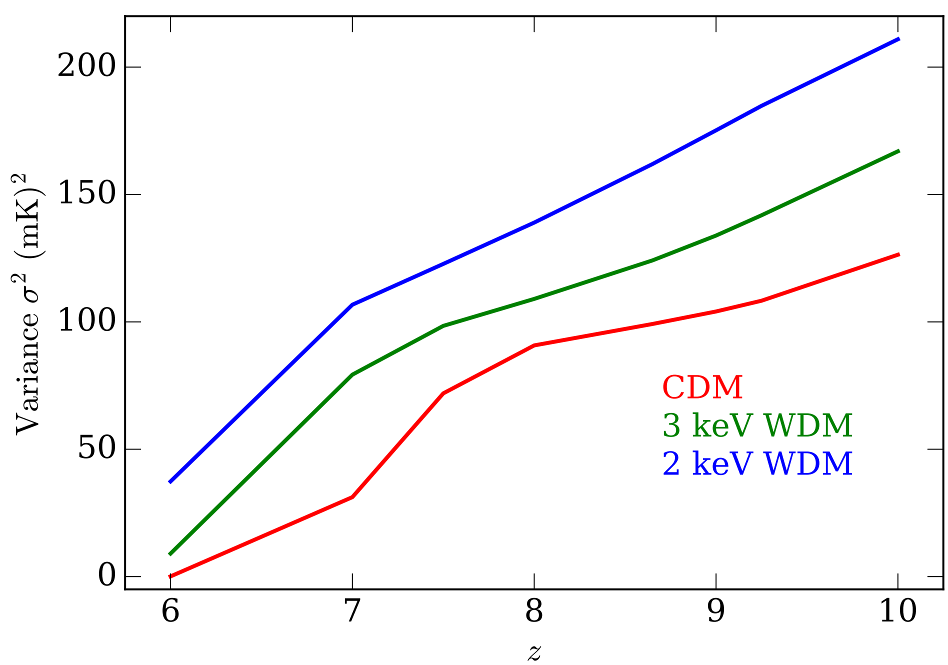


Figure 4.4: Evolution of variance of brightness temperature with redshift for CDM (red), 3 keV WDM (green) and 2 keV WDM (blue)

Table 4.1: This tabulates the $\delta T_b$ variance $\sigma^2$ corresponding to the mass averaged neutral fraction $\bar{x}_{\rm H\,I} = \{0.84, 0.64\}$ for all the models.

| Neutral fraction | Variance ($\sigma^2$) | | |
|---|---|---|---|
| $\bar{x}_{\rm H\,I}$ | CDM | 3 keV WDM | 2 keV WDM |
| 0.84 | 126.36 | 141.84 | 161.94 |
| 0.64 | 99.16 | 109.01 | 122.75 |

### 4.2.2 Skewness

It is clear from the distribution of 21-cm brightness temperature in Figure 4.3 that there is a significant non-Gaussianity present in the 21-cm signal. Initially, this non-Gaussianity is driven by the non-linear gravitational clustering and later by the growth of ionized regions which are non-randomly distributed. These non-Gaussian features of the signal will not be captured by the variance. So, we need to go for the higher-order statistics e.g. skewness. In Figure 4.5, we show the evolution of the skewness, estimated using equation (3.6), with redshift for all dark matter models.

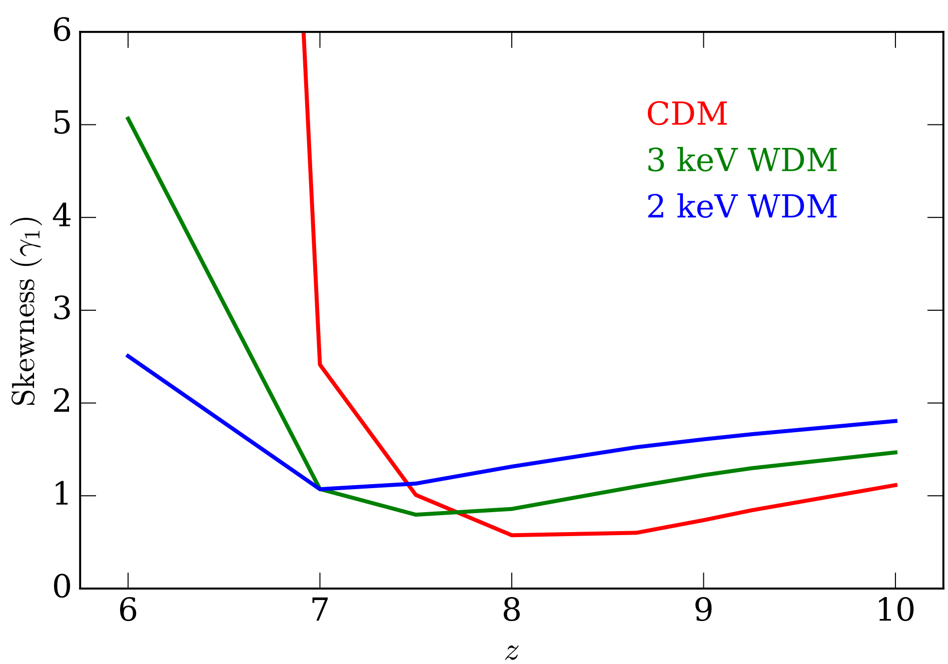


Figure 4.5: Evolution of skewness of brightness temperature with redshift for CDM (red), 3 keV WDM (green) and 2 keV WDM (blue)

We observe that the skewness $\gamma_1$ decreases with the evolving state of ionization until $\bar{x}_{\mathrm{H\,I}} \geq 0.50$ for any dark matter model. However, once the universe gets 50% ionized (e.g. $\bar{x}_{\mathrm{H\,I}} < 0.50$), the skewness increases rapidly because the zero brightness temperature spike dominates the PDF during the later stages of reionization.

Further, we tabulate the skewness at the same mass averaged neutral fraction in Table 4.2. We notice that at any stage of reionization, the skewness varies with the dark matter model as $\gamma_1$ (CDM) $<$ $\gamma_1$ (3 keV WDM) $<$ $\gamma_1$ (2 keV WDM), which is evident from the $\delta T_{\mathrm{b}}$ distribution in Figure 4.3.

Table 4.2: This tabulates the skewness $\gamma_1$ of the distribution of $\delta T_{\mathrm{b}}$ corresponding to the mass averaged neutral fraction $\bar{x}_{\mathrm{H\,I}}$ = {0.84, 0.64} for all the models.

| Neutral fraction | Skewness ($\gamma_1$) | | |
|---|---|---|---|
| $\bar{x}_{\mathrm{H\,I}}$ | CDM | 3 keV WDM | 2 keV WDM |
| 0.84 | 1.115 | 1.297 | 1.523 |
| 0.64 | 0.601 | 0.858 | 1.132 |

Our results regarding the one-point statistics of the 21-cm signal are consistent with previous studies by Harker et al. (2009); C. A. Watkinson et al. (2015). However, one should note that although these one-point statistics will give us some broad features of the signal fluctuations, these will not capture the correlation of the signal between different length scales. To capture this correlation, one should go for the Fourier statistics of signal.

## 4.3 Fourier Statistics of the signal

### 4.3.1 21-cm power spectrum

We next focus our attention to the statistic that one would use to detect the EoR 21-cm signal using radio interferometers, i.e. the power spectrum. The power spectrum quantifies the amplitude of fluctuations in the signal at different length scales. Figure 4.6 shows the power spectrum in all three dark matter scenarios (represented using three different line styles) at three different redshifts (represented using three different line colours). The evolution of the power spectra with redshift for a specific dark matter model demonstrated in Figure 4.6 follows the behaviour of an inside-out reionization (Choudhury et al. 2009; Majumdar, Mellema, et al. 2014; Mesinger et al. 2011; Mondal et al. 2017; Zahn et al. 2011), i.e. ionization starts at the highest density regions (where the ionizing sources are) in the IGM and then it gradually makes it's way to the low density regions. The kind of inside-out reionization makes power at the large scales (small $k$ modes) grow in amplitude as reionization progresses and reach its peak at $\bar{x}_{\mathrm{H\,I}} \sim 0.5$ and then go down in amplitude.

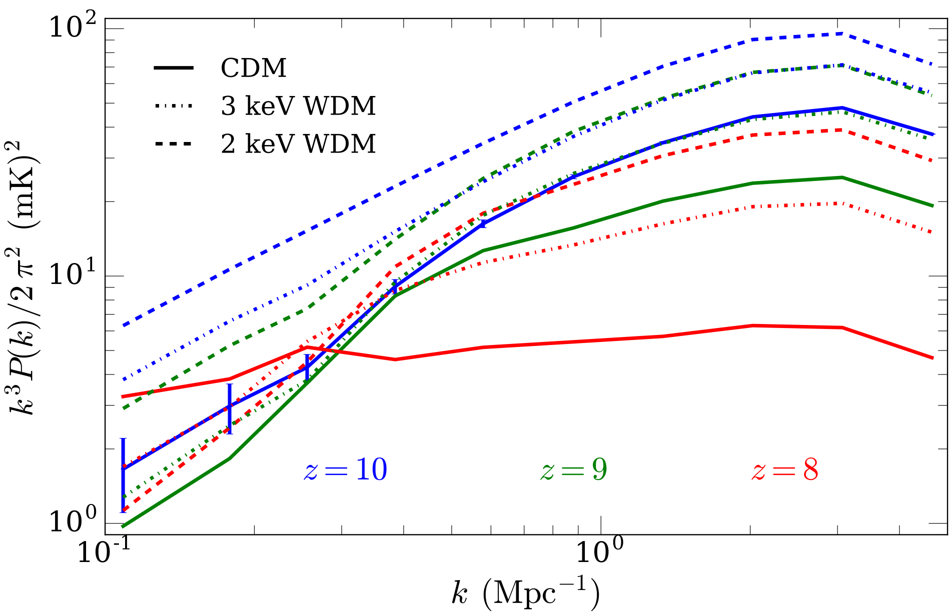


Figure 4.6: 21-cm power spectrum for CDM (solid), 3 keV WDM (dotted-dashed) and 2 keV WDM (dashed) at $z$ = 10 (blue), 9 (green) and 8 (red)

Figure 4.6 clearly shows that the difference in the 21-cm power spectra for different dark matter models is quite large (by even few orders of magnitude in certain $k$ modes), when they are compared at the same redshifts. However, even if these power spectra are at the same redshifts, they are from different stages of reionization for different dark matter models. To get a better idea of how a dark matter model impacts the reionization process it is more reasonable to compare the 21-cm statistics at the same stage of reionization (determined by the $\bar{x}_{\mathrm{H\,I}}$ value) in different dark matter models.

#### 4.3.1.1 Difference in 21-cm power spectrum between different dark matter models at same mass averaged neutral fraction

The amplitude of the redshifted 21-cm power spectrum during the EoR is determined mainly by the fluctuations in the neutral fraction ($\bar{x}_{\mathrm{H\,I}}$) field. This is why it is more logical to compare the EoR 21-cm power spectra from different dark matter models at the same stages of reionization (i.e. approximately for the same values of $\bar{x}_{\mathrm{H\,I}}$). Here the expectation is, when compared for the same values of $\bar{x}_{\mathrm{H\,I}}$, the differences in $P(k)$ will be mainly due to the differences in the 21-cm topology, rather than the overall level of ionization of the IGM or the delay in the reionization history.

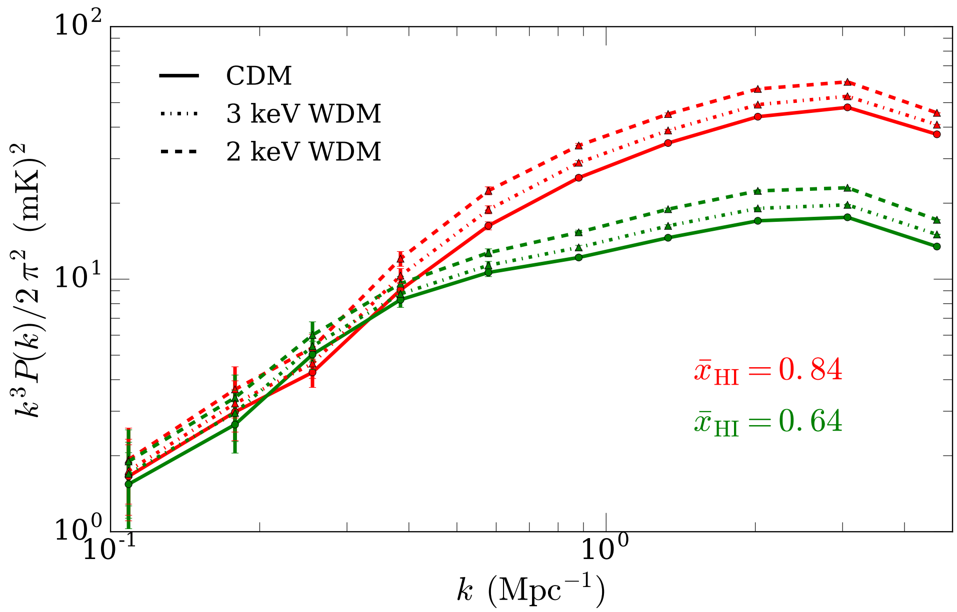


Figure 4.7: 21-cm power spectrum for CDM (solid), 3 keV WDM (dotted-dashed) and 2 keV WDM (dashed) at same mass averaged neutral fraction for $\bar{x}_{\mathrm{H\,I}}$ = 0.84 (red) and 0.64 (green)

Figure 4.7 shows the 21-cm power spectrum at approximately same averaged neutral fraction values ($\bar{x}_{\mathrm{H\,I}}$ = {0.84, 0.64}) for different dark matter models (the corresponding redshifts for different dark matter models are tabulated in Table 3.1). It is obvious from this plot that the differences in power spectra between the WDM models and the CDM model become significantly low when compared in this way, and for small $k$ modes (or large length scales), these differences are within the sample variance limits.

To quantify the differences between the EoR 21-cm power spectra from WDM and CDM scenarios, we estimate the quantity $|(P_{\rm CDM} - P_{\rm WDM})/P_{\rm CDM}|$. Figure 4.8 shows this relative fractional difference in 21-cm power spectrum estimated at same neutral fraction $\bar{x}_{\rm H\,I} = 0.84$ and 0.64 between the WDM models and the CDM model.

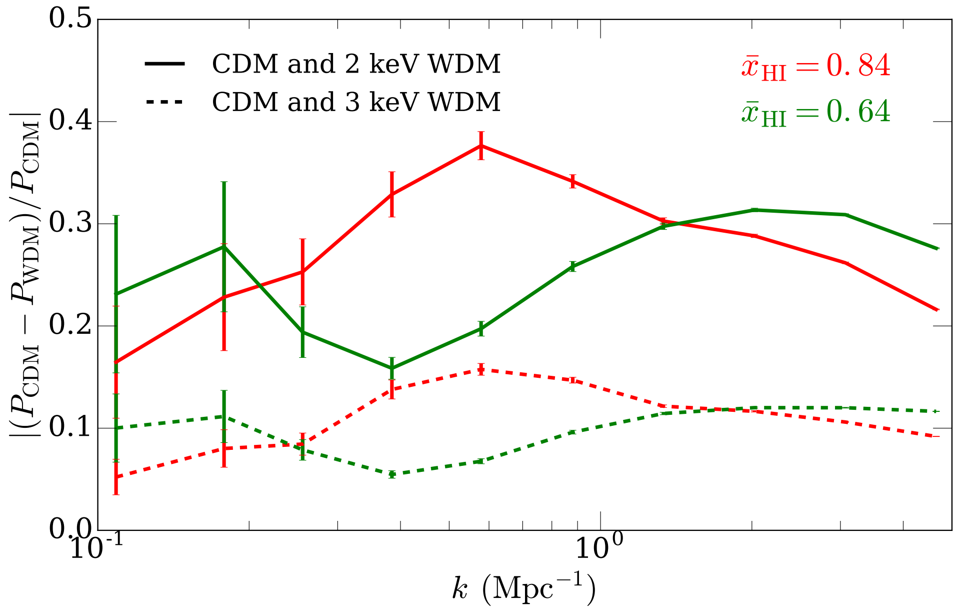


Figure 4.8: Relative fractional difference in 21-cm power spectrum between CDM and 2 keV WDM (solid), and between CDM and 3 keV WDM (dashed) estimated at $\bar{x}_{\rm H\,I} = 0.84$ (red) and 0.64 (green)

It is clear from this figure that the amplitude of this relative difference is larger for the 2 keV WDM model compared to the 3 keV WDM model. During the early stage of reionization when $\bar{x}_{\rm H\,I} = 0.84$, this difference peaks around intermediate length scales and during the intermediate stage of reionization when $\bar{x}_{\rm H\,I} = 0.64$ it is peaked around small length scales. We observe that for a large range of $k$-modes, the relative fractional difference varies in the range $0.15 - 0.35$ for the comparison between the CDM and the 2 keV WDM, and in the range $0.05 - 0.15$ for the comparison between the CDM and the 3 keV WDM model. These differences are probably not large enough to be detectable by the first generation of radio interferometers, which have lower sensitivity. These results are consistent with the previous studies made by Das et al. (2018). Thus, the power spectrum is not an ideal tool to probe the differences between different dark matter model.

### 4.3.2 21-cm bispectrum

The power spectrum is an incomplete statistics when it comes to optimally quantifying the EoR 21-cm signal fluctuations, as this signal is highly non-Gaussian. We use the next higher order statistics, the bispectrum, to quantify this evolving non-Gaussianity in the EoR 21-cm signal. The source of the non-Gaussianity in the signal is the non-random distribution of growing ionized regions in the IGM, which drives the fluctuations in the signal and also leads to the signal correlation between different length scales. We estimate signal bispectrum for all unique $k$-triangles (see Figure 3.1) for dark matter models to quantify this non-Gaussianity. Figure 4.9 shows the bispectra at three redshifts $z = \{10, 9, 8\}$, and for triangles with three $k_1$ modes $k_1 = \{0.57, 0.86, 1.30\}$ Mpc$^{-1}$. We choose not to show the bispectra for $k_1 < 0.57$ Mpc$^{-1}$ because of the high sample variance in these triangle bins (due to our small simulation volume).

In an earlier study of the EoR 21-cm bispectrum (in real space) Majumdar, Pritchard, et al. (2018) have shown that the bispectrum is mostly negative for triangles involving small $k$ modes. It has a maximum amplitude for the squeezed limit triangles (Hutter et al. 2020; Majumdar, Pritchard, et al. 2018). The bispectrum also shows a very interesting feature, it changes its sign when one gradually move from smaller $k$-triangles to triangles with larger $k$ modes. This makes the EoR 21-cm bispectra an even more interesting statistic for a confirmative detection of the signal (Hutter et al. 2020; Majumdar, Pritchard, et al. 2018). However all of these analysis was based on a few specific types of $k$-triangles and for the signal in real space. For a thorough analysis of the EoR 21-cm bispectra for all unique $k$-triangles in redshift space the readers are requested to refer to Majumdar et al. (in prep.).

Based on the plots in Figure 4.9 and the analysis of Majumdar, Pritchard, et al. (2018) and Majumdar et al. (in prep) one can identify few more generic features of the inside-out EoR 21-cm bispectra in the entire unique $k$-triangle space (defined by parameters $n$ and $\cos\theta$), irrespective of the underlying dark matter model.

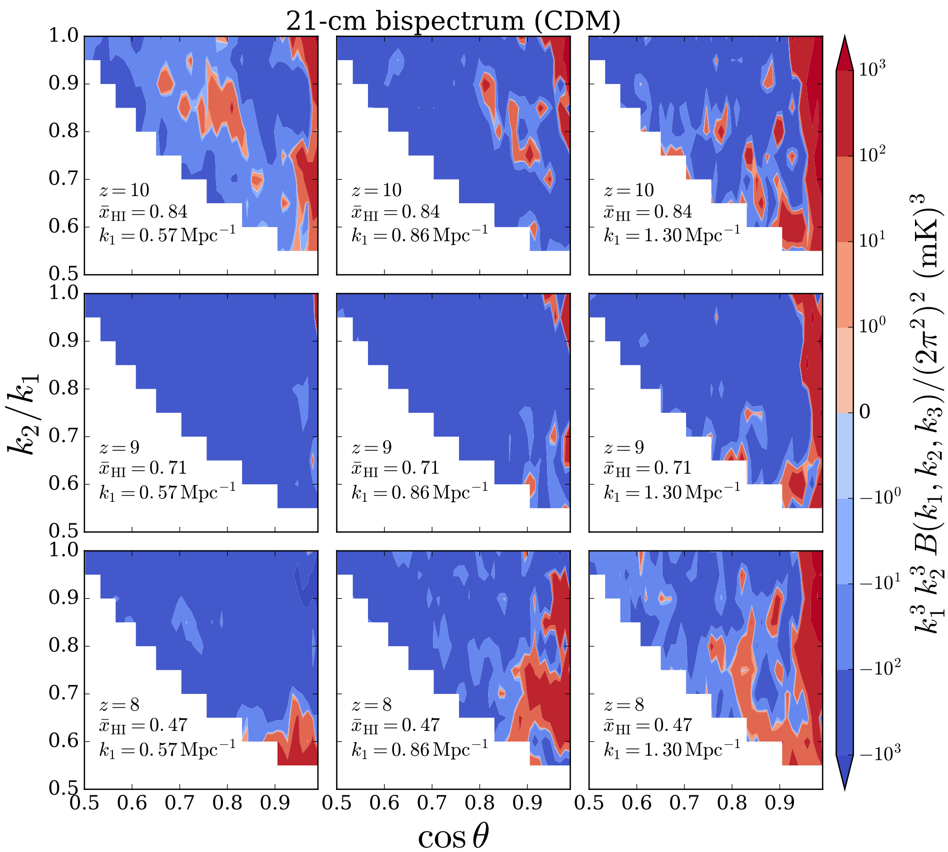
21-cm bispectrum (CDM)
$k_2/k_1$
$\cos\theta$
$z=10$, $\bar{x}_{\rm HI}=0.84$, $k_1=0.57\,{\rm Mpc}^{-1}$
$z=10$, $\bar{x}_{\rm HI}=0.84$, $k_1=0.86\,{\rm Mpc}^{-1}$
$z=10$, $\bar{x}_{\rm HI}=0.84$, $k_1=1.30\,{\rm Mpc}^{-1}$
$z=9$, $\bar{x}_{\rm HI}=0.71$, $k_1=0.57\,{\rm Mpc}^{-1}$
$z=9$, $\bar{x}_{\rm HI}=0.71$, $k_1=0.86\,{\rm Mpc}^{-1}$
$z=9$, $\bar{x}_{\rm HI}=0.71$, $k_1=1.30\,{\rm Mpc}^{-1}$
$z=8$, $\bar{x}_{\rm HI}=0.47$, $k_1=0.57\,{\rm Mpc}^{-1}$
$z=8$, $\bar{x}_{\rm HI}=0.47$, $k_1=0.86\,{\rm Mpc}^{-1}$
$z=8$, $\bar{x}_{\rm HI}=0.47$, $k_1=1.30\,{\rm Mpc}^{-1}$
$k_1^3\,k_2^3\,B(k_1,k_2,k_3)/(2\pi^2)^2\ ({\rm mK})^3$

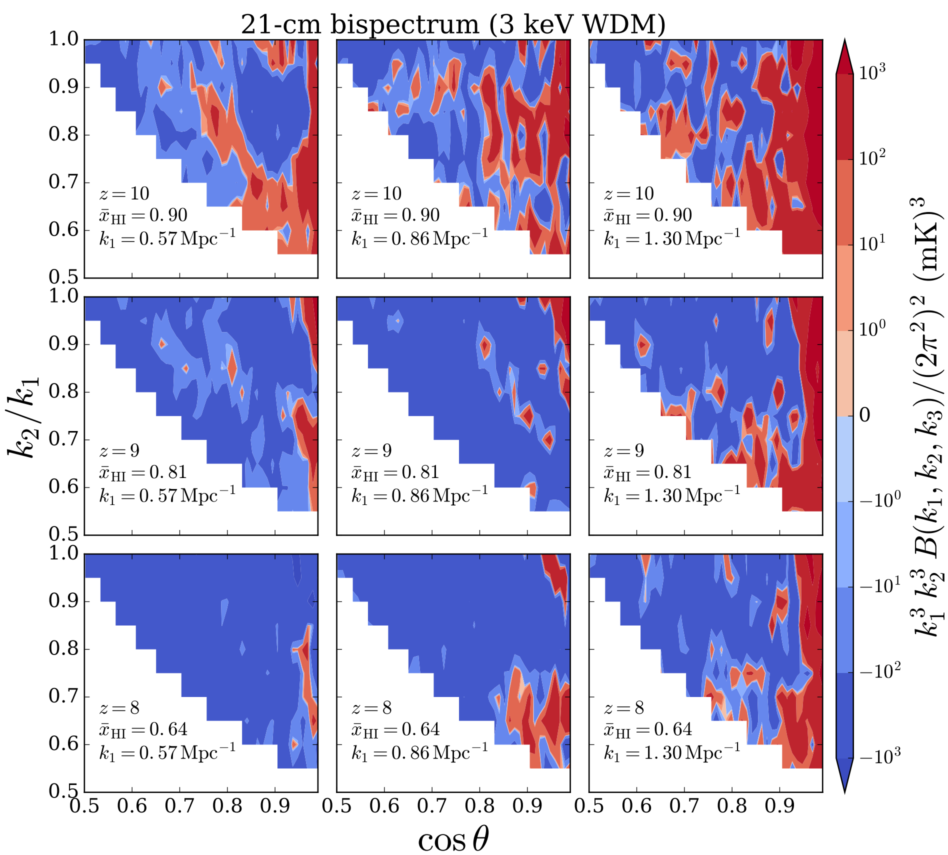
21-cm bispectrum (3 keV WDM)
$k_2/k_1$
$\cos\theta$
$z=10$, $\bar{x}_{\rm HI}=0.90$, $k_1=0.57\,{\rm Mpc}^{-1}$
$z=10$, $\bar{x}_{\rm HI}=0.90$, $k_1=0.86\,{\rm Mpc}^{-1}$
$z=10$, $\bar{x}_{\rm HI}=0.90$, $k_1=1.30\,{\rm Mpc}^{-1}$
$z=9$, $\bar{x}_{\rm HI}=0.81$, $k_1=0.57\,{\rm Mpc}^{-1}$
$z=9$, $\bar{x}_{\rm HI}=0.81$, $k_1=0.86\,{\rm Mpc}^{-1}$
$z=9$, $\bar{x}_{\rm HI}=0.81$, $k_1=1.30\,{\rm Mpc}^{-1}$
$z=8$, $\bar{x}_{\rm HI}=0.64$, $k_1=0.57\,{\rm Mpc}^{-1}$
$z=8$, $\bar{x}_{\rm HI}=0.64$, $k_1=0.86\,{\rm Mpc}^{-1}$
$z=8$, $\bar{x}_{\rm HI}=0.64$, $k_1=1.30\,{\rm Mpc}^{-1}$
$k_1^3\,k_2^3\,B(k_1,k_2,k_3)/(2\pi^2)^2\ ({\rm mK})^3$

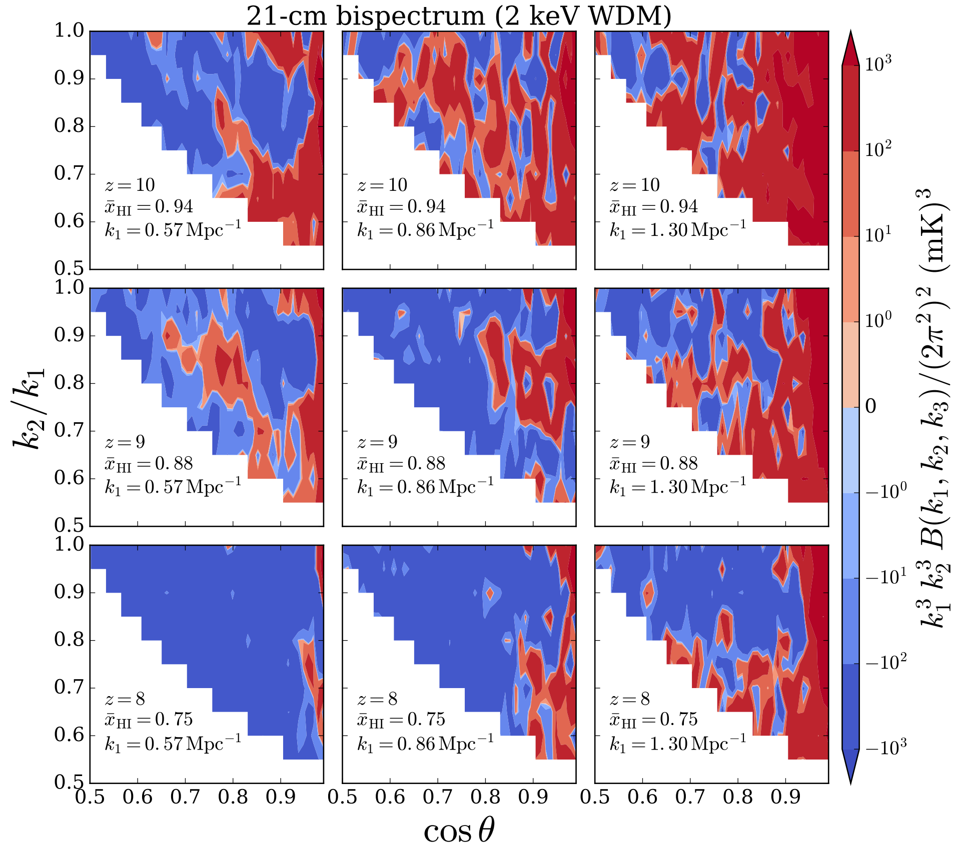


Figure 4.9: Simulated 21-cm bispectrum for all unique triangles for CDM (top panel), 3 keV WDM (central panel) and 2 keV WDM model (bottom panel) at $z = 10$, 9 and 8 (top to bottom) and for $k_1 = 0.57$, 0.86 and 1.30 $\text{Mpc}^{-1}$ (left to right). The neutral fraction at these $z$ is shown in the figure.

At the very beginning of reionization ($\bar{x}_{\rm H\,I} \geq 0.90$) for smaller $k_1$-triangles bispectra for a significant fraction of the $n - \cos\theta$ parameter space is positive and in the rest of the parameter space it is negative. For the small $k_1$-triangles as reionization progresses bispectra in most of the $n - \cos\theta$ parameter space becomes negative ($0.85 \geq \bar{x}_{\rm H\,I} \geq 0.60$) and stays negative until the $\bar{x}_{\rm H\,I} \leq 0.40$. At neutral fractions lower than this the bispectrum starts become positive again in significant portion of the triangle parameter space. Further, for a fixed $\bar{x}_{\rm H\,I}$ value as one gradually moves from smaller to larger $k_1$-triangles, a even larger fraction of the $n - \cos\theta$ space starts to have positive bispectrum. The bispectra start to become positive mainly near the squeezed and linear limits ($\cos\theta \simeq 1$) of triangles at almost during all stages of the reionization. The amplitude of the bispectra for small $k_1$-triangles reaches a maximum when $\bar{x}_{\rm H\,I} \sim 0.5$.

The evolution of sign and amplitude of the bispectra can be interpreted in the light of quasi-linear model of brightness temperature fluctuations (Mao et al. 2012). Using this model one can show that there are total eight component bispectra (two auto and six cross) that contributes to the redshift space EoR 21-cm bispectra. Among these eight components the most important ones for the small $k_1$-triangles are the two auto bispectrum of the H I and the matter density field and three cross-bispectra between H I and matter density fields. These components make the 21-cm bispectra negative in most of the parameter space. The contribution from auto bispectrum of the matter density field is negligible for small $k_1$-triangles. As one moves towards the bispectra for large $k_1$-triangles contribution from the auto bispectrum of the matter density field (which is always positive in sign for all types of triangles) grows and become significantly large at largest $k_1$-triangles and make the 21-cm bispectra positive. For a more detailed discussion on this topic we refer the reader to Majumdar et al. (in prep).

Figure 4.9 clearly shows that if one compares the bispectra for different dark matter models at the same redshifts, as expected, the differences between them would be quite large. For some $k$-triangles and depending on the stages of the reionization these relative differences can be even larger than the ones observed in case of power spectra. This is due to the fact that as the stages of the reionization are different for different models, the over all level of fluctuations as well the topology will be significantly different, both of which affects the bispectrum amplitude and sign.

#### 4.3.2.1 Difference in 21-cm bispectrum between different dark matter models at same mass averaged neutral fraction

For the similar reasons as discussed in case of the power spectra, here also we compare the bispectra for different dark matter models approximately at the same stages of reionization (i.e. $\bar{x}_{\rm H\,I} = 0.84$ and 0.64). We estimate the relative differences in the bispectra between the CDM and WDM models by computing the quantity $|(B_{\rm CDM} - B_{\rm WDM})/B_{\rm CDM}|$ (Figure 4.10).

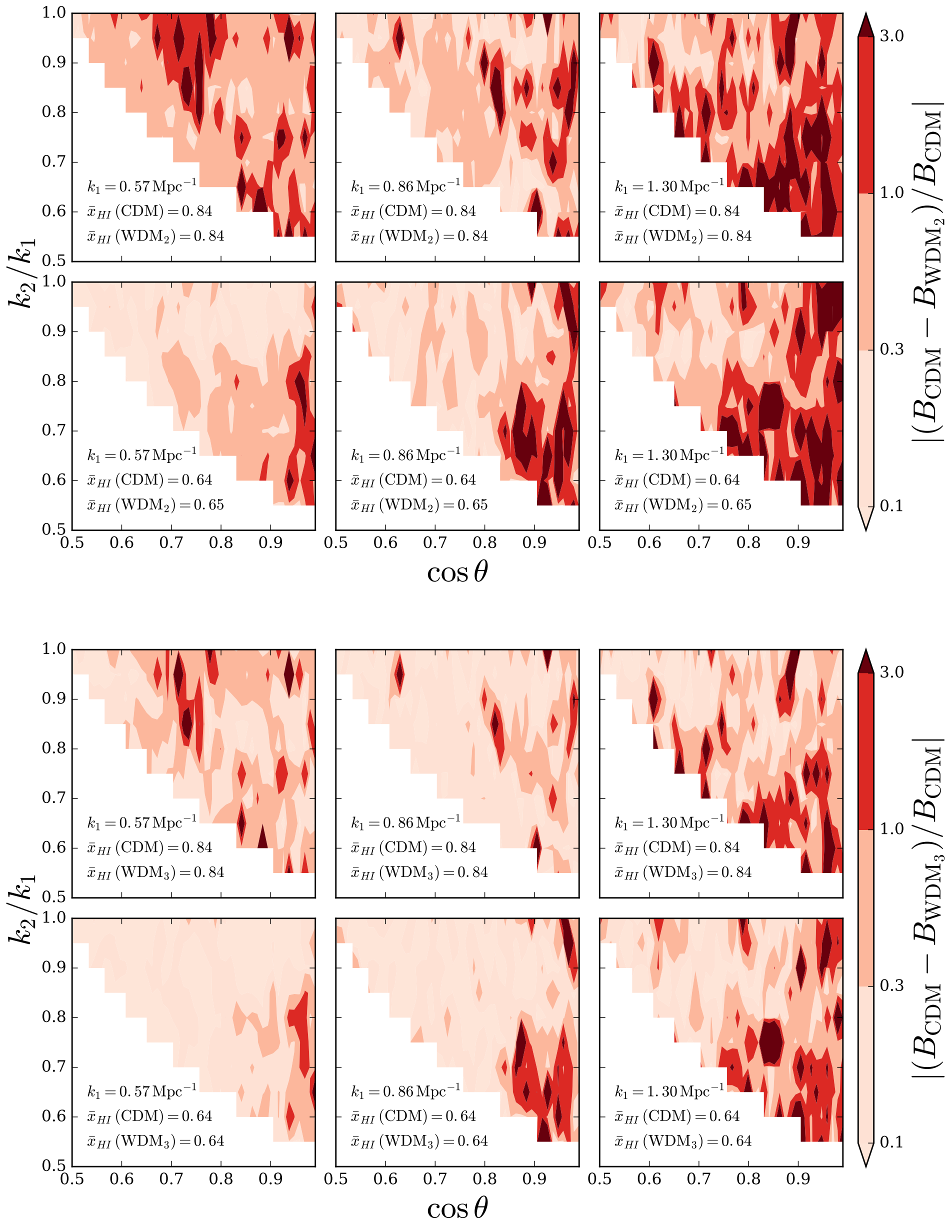


Figure 4.10: Relative fractional difference in 21-cm bispectrum between CDM and 2 keV WDM model (top panel), and between CDM and 3 keV WDM model (bottom panel) for $k_1$ = 0.57, 0.86 and 1.30 Mpc$^{-1}$ (left to right) at same mass averaged neutral fraction with $\bar{x}_{\rm H\,I} = 0.84$ and 0.64

It is apparent from Figure 4.10 that at any stage of reionization, the differences between the 2 keV WDM and CDM models is larger than the differences between the 3 keV WDM and CDM models. For most of the $k$-triangle parameter space ($n - \cos\theta$ space) the relative difference between the

2 keV WDM and CDM models is in between $30-300\%$ or more and for the 3 keV WDM and CDM models the same is in between $10-100\%$ or more. These differences are more prominent for triangles with larger $k_1$ modes compared to the triangles with smaller $k_1$ modes. They are particularly large in the region of the $n-\cos\theta$ space where $n \leq 0.75$ and $0.75 \leq \cos\theta \leq 1.0$.

One important point to note here is that, though we are looking at the 21-cm statistics at almost same stages of reionization in different dark matter models, as the redshifts are different the underlying halo characteristics and distribution will vary from model to model (which can be quantified by their halo mass functions). This differences in the halo mass, their numbers and their spatial distribution will lead to a difference in 21-cm topology across the dark matter models, even when the overall level of ionization remains more or less same in all of these cases. The 21-cm signal power spectrum is expected to be not very sensitive to these differences in topology, however the signal bispectrum will be very sensitive to them as these differences in topology leads to a significant difference in the non-Gaussian characteristics of the signal. One can expect that these significantly larger relative differences in the signal bispectra (compared to their relative differences in power spectra), when the underlying dark matter model is different, will be possible to detect with the upcoming highly sensitive SKA. Using sophisticated parameter estimation techniques, while using the signal bispectra as the target statistic, one may be even able to constrain the nature of the dark matter from such future radio interferometric observations of the EoR.

## 4.4 Analysis with different ionizing efficiency $N_{\rm ion}$ for different dark matter models

In this section, we repeat our analysis by varying the ionizing efficiency parameter $N_{\rm ion}$ in different dark matter models to ensure that we obtain the same $\bar{x}_{\rm H\,I}$ for all of these models in the same redshifts. We choose the $N_{\rm ion}$ values such that (Table 4.3) in all models universe becomes 50% ionized by redshift 8.

Table 4.3: This tabulates the $N_{\text{ion}}$ values required in different dark matter models to ensure that $\bar{x}_{\text{H I}} \approx 0.5$ at $z = 8$.

| CDM | 3 keV WDM | 2 keV WDM |
|---|---|---|
| 23.21 | 33.70 | 47.50 |

### 4.4.1 21-cm topology

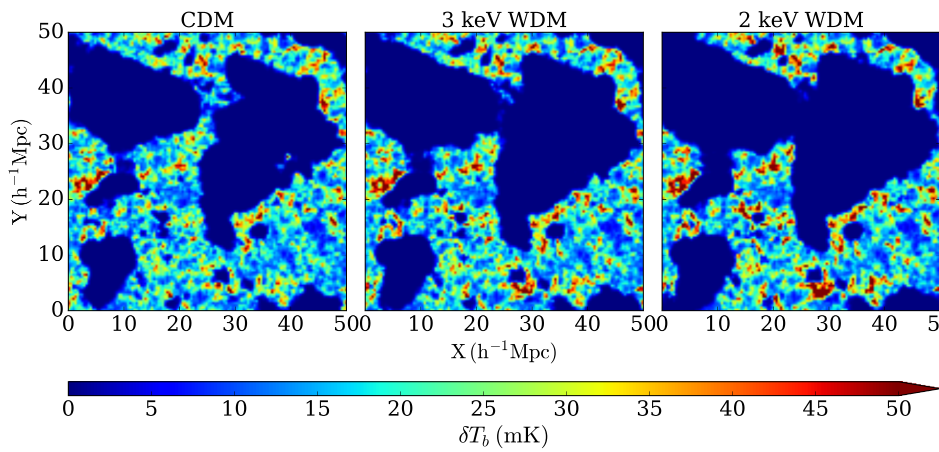


Figure 4.11: 21-cm brightness temperature maps at $z = 8$ with same mass averaged neutral fraction $\bar{x}_{\text{H I}} = 0.47$ for CDM (left), 3 keV WDM (middle) and 2 keV WDM (right) model

In Figure 4.11, we have shown the 21-cm brightness temperature maps at $z = 8$ with mass averaged neutral fraction $\bar{x}_{\text{H I}} \approx 0.5$ for all the models. We observe that the 21-cm topology has significant similarity at large scales, however, it has quite a few differences at small length scales for different models of dark matter. The size of ionized bubbles is relatively larger in WDM models compared to the CDM model. This is an obvious signature of the suppression in the number of low mass halos in WDM models compared to their CDM counterpart. The lack of the low mass halos have been compensated by increasing the ionizing photon production efficiency (see Table 4.3) in all halos in these models. This implies that the high mass halos in WDM models will produce significantly more photons compared to their counterparts in CDM model and will thus produce larger ionized bubbles (compare the three panels in Figure 4.11). These features have also been reported by Das et al. (2018).

### 4.4.2 Observable statistics of the 21-cm signal

#### 4.4.2.1 21-cm power spectrum

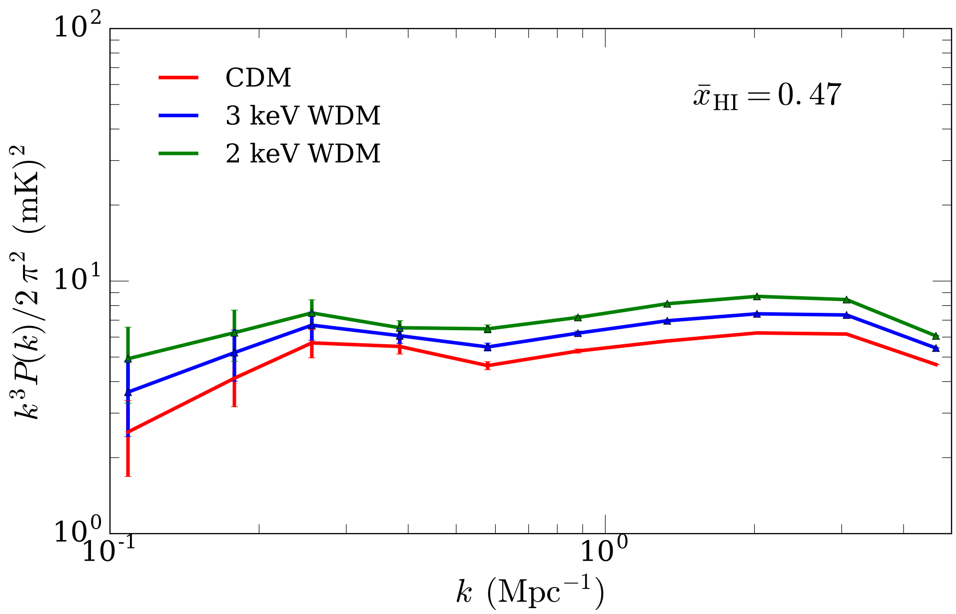


Figure 4.12: 21-cm power spectrum at $z = 8$ with mean neutral fraction $\bar{x}_{\rm H\,I} = 0.47$ in CDM (red), 3 keV WDM (blue) and 2 keV WDM (green)

Figure 4.12 shows the 21-cm power spectrum for different dark matter models at $\bar{x}_{\rm H\,I} \approx 0.5$. We observe that the 21-cm power spectrum in WDM models is greater than that in the CDM model. This is because in WDM models, the ionized bubbles are larger in size (due to the increased $N_{\rm ion}$ value). One can also notice that the difference in 21-cm power spectra between different models remains significantly low even if we change our reionization model, and at large scales these differences are within the sample variance limit.

#### 4.4.2.2 21-cm bispectrum

In Figure 4.13, we have shown the relative fractional difference in 21-cm bispectra between the CDM and WDM models at $k_1 = 0.57$, 0.86 and 1.30 Mpc$^{-1}$. One obvious observation that one can make is that these differences in bispectra are larger when estimated between CDM and 2 keV WDM model.

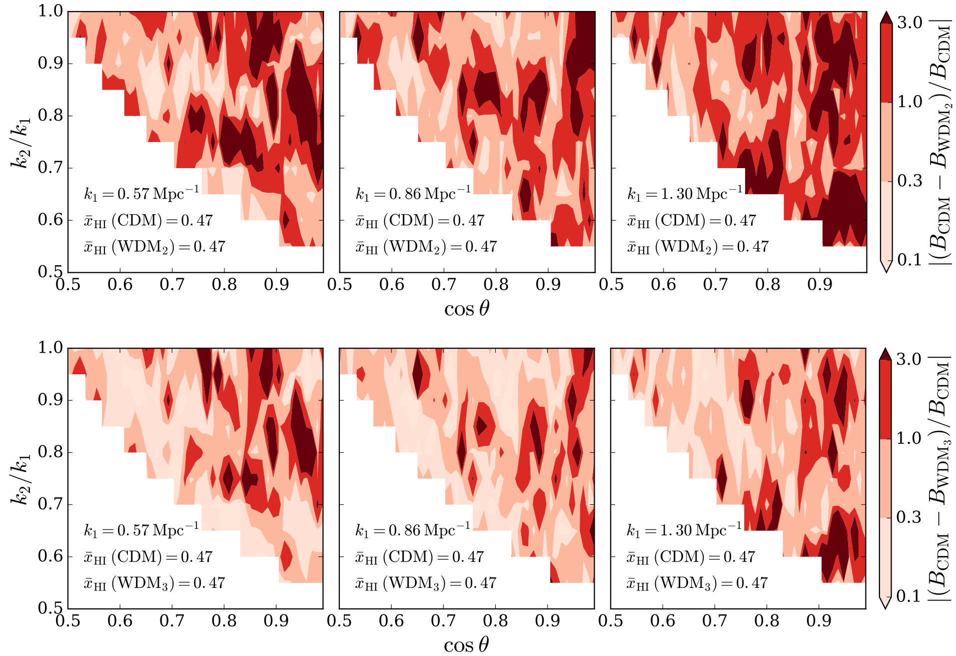


Figure 4.13: Relative fractional difference in 21-cm bispectra between CDM and 2 keV WDM model (top panel), and between CDM and 3 keV WDM model (bottom panel) at the same mass averaged neutral fraction $\bar{x}_{\mathrm{H\,I}} = 0.47$

Further, these differences are larger than those observed in Figure 4.10. This is because by changing the $N_{\mathrm{ion}}$, we are changing our reionization model. Note that even at large scales $k_1 = 0.57$ Mpc$^{-1}$, the differences are large for most of the unique $k$ triangles. Additionally, at relevant small scales (or large $k_1$ values), the differences are also quite large due to the fact that the strength of 21-cm signal gets increased in WDM models at small scales.

We conclude that even when one changes the reionization source model to arrive at same state of IGM ionization at the same redshift for different dark matter models, the bispectrum remains equally or more sensitive to the characteristics of the dark matter model. However, power spectrum remains equally insensitive to the dark matter model characteristics in this case as well.

# Chapter 5

# Summary

In this thesis, we have quantified the impact of the different kind of warm dark matter models (in comparison with the standard cold dark matter models) on the reionization process and related 21-cm observables such as the power spectrum and bispectrum. We have considered 2 keV and 3 keV thermal WDM models in this context. Using GADGET 2.0 N-body simulations, we observed that the non-negligible free streaming of the dark matter particles in warm dark matter scenarios suppresses the matter density perturbations on small scales (Figure 2.3). Further, this suppression was more prominent in the 2 keV WDM scenario compared to the 3 keV WDM model because the lighter the WDM particle, the larger the free streaming scale. We also observed that the effect of this suppressed structure formation gets reflected in the halo mass function of all the dark matter models (see Figure 2.4).

Using a semi-numerical model for reionization, we further observed that due to this suppression of the low mass haloes (which are the dominant sources of ionizing photons), the overall reionization of the universe gets delayed in WDM scenarios compared to the CDM model (Figure 4.1). This delay is likewise larger in the 2 keV WDM model compared to the 3 keV WDM model, when one keeps the ionizing photon production efficiency of haloes the same in all dark matter models. The suppression of low mass haloes additionally introduces a significant difference in 21-cm brightness temperature topology in case of WDM models compared to the CDM model (see Figure 4.2).

Next, we have quantified the differences in the two observable statistics of the EoR 21-cm signal, power spectrum and bispectrum, for different dark matter models. We found that, if the statistics from different dark models are compared at the same redshifts, the power spectrum differs significantly for both small and large $k$ modes for different matter models (Figure 4.6). However, when they are compared at the same stage of reionization i.e. at same $\bar{x}_{\rm H\,I}$ (i.e. by countering the effect of delayed reionization history), the differences in the $P(k)$ become significantly small at all scales between the WDM and CDM models. The relative differences between the EoR 21-cm power spectra for CDM and WDM models varies between $5\% - 35\%$ (see Figure 4.8). These differences become undetectable in case of small $k$ modes as they fall within the sample variance limits.

We have, for the first time, quantified the impact of WDM models on the EoR 21-cm signal using the bispectrum. The bispectrum is expected to be more sensitive to the difference in the dark matter model as it is capable of capturing the non-Gaussian features in the signal to which power spectrum is not sensitive. The source of non-Gaussianity in the EoR 21-cm signal is the evolving H I topology during this period, which gets significantly affected by the suppression of the low mass haloes in case of the WDM models. We find that the relative differences between the 21-cm bispectra for the WDM and CDM models are larger than their relative differences in the 21-cm power spectrum when compared at the same redshifts (Figure 4.9). Even when compared at the same stages of reionization, the relative differences between the EoR 21-cm bispectra for WDM and CDM models varies between $10\% - 300\%$ for all unique $k$-triangles (see Figure 4.10). This level of relative differences in 21-cm bispectra for most of the unique $k$-triangle parameter space ensures that one should be able distinguish between the different dark matter models using the future radio interferometric observations of the EoR and this may even help one to constrain the WDM model parameters.

Through this analysis we have established that the redshifted 21-cm bispectra is a unique and much more sensitive statistics than the power spectrum for differentiating the impact of different models of dark matter on the reionization process and one may be able to constrain the nature of the dark matter using this statistic from future observations of the CD-EoR through the SKA.

Note that in this work we have not taken into account the impact of spin temperature fluctuations on the EoR 21-cm signal, which may have a significant effect on the 21-cm bispectrum. We have considered only a single model for reionization. However, the 21-cm topology and the resulting non-Gaussianity in the signal may change significantly if we change our reionization model. All of these effects will affect the 21-cm bispectrum. However, even if we take into account all of these effects into our formalism for a more accurate model of the EoR 21-cm signal, we expect that the differences in different dark matter models will still be prominently visible in the 21-cm bispectra.

# Chapter 6

# Future Scope

The work presented in this thesis could be further extended in several directions. We discuss some of the possible extension below.

- In this work, we have estimated different observable statistics of the 21-cm signal by simulating the signal in a volume of [50 $\mathrm{h}^{-1}$ Mpc]$^3$. However, the convergence of different signal statistics (specifically at large length scales or small $k$ modes) require the signal to be simulated in a larger volume $\geq$ [100 Mpc]$^3$. The volume of our simulation was limited by the total memory (RAM) available to us in our computing resources. To simulate a cosmological volume $\geq$ [100 Mpc]$^3$ with the same mass resolution that has been used here we will need $\geq$ 1 TB RAM. We plan to address this issue in future when we have access to computing facilities which satisfies the above minimum memory requirements.

- In our formalism presented here, we have assumed that there has been perfect foreground removal from the data and there is no system noise present in the data either. It would be interesting to see how well one can distinguish the impact of different dark matter models on the 21-cm signal statistics when there is a certain amount of residual foregrounds left in the data and also the uncertainties due to the presence of noise is taken into account.

- To better understand how the differences in dark matter model impacts the halo distribution and their evolution and in turn the 21-cm topology, it would be interesting to estimate the cross-bispectra between the 21-cm field and the halo field for different models. Presently, we are working on this particular extension.

- In this thesis we have shown the impact of different dark matter models on different Fourier statistics of the EoR 21-cm signal. We have quantified the impact of different dark matter models by calculating relative differences in these statistics (compared to the CDM model). However, in reality one would having only one universe with only one dark matter model, so estimation of this kind of relative difference in 21-cm statistics between different dark matter models will not be possible. To identify the underlying dark matter model one would need to perform a Bayesian model selection analysis of the observable 21-cm statistics. The model selection exercise will involve considering all kinds of dark matter models as well as one will also exploring the entire reionization parameter space. We plan to proceed in this direction in future.

# Bibliography


Abazajian, K., Fuller, G. M., & Patel, M. (2001). Sterile neutrino hot, warm, and cold dark matter., *64*(2), arXiv astro-ph/0101524, 023501. https://doi.org/10.1103/PhysRevD.64.023501

Arcadi, G., Dutra, M., Ghosh, P., Lindner, M., Mambrini, Y., Pierre, M., Profumo, S., & Queiroz, F. S. (2018). The waning of the WIMP? A review of models, searches, and constraints. *European Physical Journal C*, *78*(3), arXiv 1703.07364, 203. https://doi.org/10.1140/epjc/s10052-018-5662-y

Barkana, R., & Loeb, A. (2001). In the beginning: the first sources of light and the reionization of the universe., *349*(2), arXiv astro-ph/0010468, 125–238. https://doi.org/10.1016/S0370-1573(01)00019-9

Barry, N., Wilensky, M., Trott, C. M., Pindor, B., Beardsley, A. P., Hazelton, B. J., Sullivan, I. S., Morales, M. F., Pober, J. C., Line, J., Greig, B., Byrne, R., Lanman, A., Li, W., Jordan, C. H., Joseph, R. C., McKinley, B., Rahimi, M., Yoshiura, S., . . . Wyithe, J. S. B. (2019). Improving the Epoch of Reionization Power Spectrum Results from Murchison Widefield Array Season 1 Observations., *884*(1), arXiv 1909.00561, 1. https://doi.org/10.3847/1538-4357/ab40a8

Bergström, L. (2009). Dark matter candidates. *New Journal of Physics*, *11*(10), arXiv 0903.4849, 105006. https://doi.org/10.1088/1367-2630/11/10/105006

Bertone, G., Hooper, D., & Silk, J. (2005). Particle dark matter: evidence, candidates and constraints., *405*(5-6), arXiv hep-ph/0404175, 279–390. https://doi.org/10.1016/j.physrep.2004.08.031

Bharadwaj, S., Mazumdar, A., & Sarkar, D. (2020). Quantifying the Redshift Space Distortion of the Bispectrum I: Primordial Non-Gaussianity., arXiv 2001.10243. https://doi.org/10.1093/mnras/staa279

Bharadwaj, S., & Pandey, S. K. (2005). Probing non-Gaussian features in the HI distribution at the epoch of re-ionization., *358*(3), arXiv astro-ph/0410581, 968–976. https://doi.org/10.1111/j.1365-2966.2005.08836.x

Bode, P., Ostriker, J. P., & Turok, N. (2001). Halo Formation in Warm Dark Matter Models., *556*(1), arXiv astro-ph/0010389, 93–107. https://doi.org/10.1086/321541

Boera, E., Becker, G. D., Bolton, J. S., & Nasir, F. (2019). Revealing Reionization with the Thermal History of the Intergalactic Medium: New Constraints from the Ly$\alpha$ Flux

Power Spectrum., *872*(1), arXiv 1809.06980, 101. https://doi.org/10.3847/1538-4357/aafee4

Bowman, J. D., Rogers, A. E. E., Monsalve, R. A., Mozdzen, T. J., & Mahesh, N. (2018). An absorption profile centred at 78 megahertz in the sky-averaged spectrum., *555*(7694), arXiv 1810.05912, 67–70. https://doi.org/10.1038/nature25792

Boyarsky, A., Drewes, M., Lasserre, T., Mertens, S., & Ruchayskiy, O. (2019). Sterile neutrino Dark Matter. *Progress in Particle and Nuclear Physics*, *104*arXiv 1807.07938, 1–45. https://doi.org/10.1016/j.ppnp.2018.07.004

Brandbyge, J., & Hannestad, S. (2017). Cosmological N-body simulations with generic hot dark matter., *2017*(10), arXiv 1706.00025, 015. https://doi.org/10.1088/1475-7516/2017/10/015

Bromm, V., Coppi, P. S., & Larson, R. B. (2002). The Formation of the First Stars. I. The Primordial Star-forming Cloud., *564*(1), arXiv astro-ph/0102503, 23–51. https://doi.org/10.1086/323947

Bromm, V., & Larson, R. B. (2004). The First Stars., *42*(1), arXiv astro-ph/0311019, 79–118. https://doi.org/10.1146/annurev.astro.42.053102.134034

Bullock, J. S., & Boylan-Kolchin, M. (2017). Small-Scale Challenges to the $\Lambda$CDM Paradigm., *55*(1), arXiv 1707.04256, 343–387. https://doi.org/10.1146/annurev-astro-091916-055313

Burns, J. O., Bradley, R., Tauscher, K., Furlanetto, S., Mirocha, J., Monsalve, R., Rapetti, D., Purcell, W., Newell, D., Draper, D., MacDowall, R., Bowman, J., Nhan, B., Wollack, E. J., Fialkov, A., Jones, D., Kasper, J. C., Loeb, A., Datta, A., . . . Bicay, M. (2017). A Space-based Observational Strategy for Characterizing the First Stars and Galaxies Using the Redshifted 21 cm Global Spectrum., *844*(1), arXiv 1704.02651, 33. https://doi.org/10.3847/1538-4357/aa77f4

Carucci, I. P., Corasaniti, P.-S., & Viel, M. (2017). Imprints of non-standard dark energy and dark matter models on the 21cm intensity map power spectrum., *2017*(12), arXiv 1706.09462, 018. https://doi.org/10.1088/1475-7516/2017/12/018

Carucci, I. P., Villaescusa-Navarro, F., Viel, M., & Lapi, A. (2015). Warm dark matter signatures on the 21cm power spectrum: intensity mapping forecasts for SKA., *2015*(7), arXiv 1502.06961, 047. https://doi.org/10.1088/1475-7516/2015/07/047

Choudhury, T. R., Haehnelt, M. G., & Regan, J. (2009). Inside-out or outside-in: the topology of reionization in the photon-starved regime suggested by Ly$\alpha$ forest data., *394*(2), arXiv 0806.1524, 960–977. https://doi.org/10.1111/j.1365-2966.2008.14383.x

Ciardi, B. [B.], Bianchi, S., & Ferrara, A. (2002). Lyman continuum escape from an inhomogeneous interstellar medium., *331*(2), arXiv astro-ph/0111532, 463–473. https://doi.org/10.1046/j.1365-8711.2002.05194.x

Ciardi, B. [Benedetta], & Ferrara, A. (2005). The First Cosmic Structures and Their Effects., *116*(3-4), arXiv astro-ph/0409018, 625–705. https://doi.org/10.1007/s11214-005-3592-0

Corasaniti, P. S., Agarwal, S., Marsh, D. J. E., & Das, S. (2017). Constraints on dark matter scenarios from measurements of the galaxy luminosity function at high redshifts. *Phys. Rev. D*, *95*, 083512. https://doi.org/10.1103/PhysRevD.95.083512

Das, S., Mondal, R., Rentala, V., & Suresh, S. (2018). On dark matter-dark radiation interaction and cosmic reionization., *2018*(8), arXiv 1712.03976, 045. https://doi.org/10.1088/1475-7516/2018/08/045

Dayal, P., Choudhury, T. R., Bromm, V., & Pacucci, F. (2017). Reionization and Galaxy Formation in Warm Dark Matter Cosmologies., *836*(1), arXiv 1501.02823, 16. https://doi.org/10.3847/1538-4357/836/1/16

Del Popolo, A., & Le Delliou, M. (2017). Small Scale Problems of the ΛCDM Model: A Short Review. *Galaxies*, *5*(1), arXiv 1606.07790, 17. https://doi.org/10.3390/galaxies5010017

Diemand, J., & Moore, B. (2011). The Structure and Evolution of Cold Dark Matter Halos. *Advanced Science Letters*, *4*(2), arXiv 0906.4340, 297–310. https://doi.org/10.1166/asl.2011.1211

Dijkstra, M., Haiman, Z., & Spaans, M. (2006). Ly$\alpha$ Radiation from Collapsing Protogalaxies. I. Characteristics of the Emergent Spectrum., *649*(1), arXiv astro-ph/0510407, 14–36. https://doi.org/10.1086/506243

Dodelson, S., & Widrow, L. M. (1994). Sterile neutrinos as dark matter., *72*(1), arXiv hep-ph/9303287, 17–20. https://doi.org/10.1103/PhysRevLett.72.17

Fan, X., Carilli, C. L., & Keating, B. (2006). Observational Constraints on Cosmic Reionization., *44*(1), arXiv astro-ph/0602375, 415–462. https://doi.org/10.1146/annurev.astro.44.051905.092514

Faucher-Giguère, C.-A., Kereš, D., Dijkstra, M., Hernquist, L., & Zaldarriaga, M. (2010). Ly$\alpha$ Cooling Emission from Galaxy Formation., *725*(1), arXiv 1005.3041, 633–657. https://doi.org/10.1088/0004-637X/725/1/633

Feng, J. L. (2010). Dark Matter Candidates from Particle Physics and Methods of Detection., *48*arXiv 1003.0904, 495–545. https://doi.org/10.1146/annurev-astro-082708-101659

Frenk, C. S., & White, S. D. M. (2012). Dark matter and cosmic structure. *Annalen der Physik*, *524*(9-10), arXiv 1210.0544, 507–534. https://doi.org/10.1002/andp.201200212

Furlanetto, S. R., & Loeb, A. (2002). The 21 Centimeter Forest: Radio Absorption Spectra as Probes of Minihalos before Reionization., *579*(1), arXiv astro-ph/0206308, 1–9. https://doi.org/10.1086/342757

Furlanetto, S. R., Oh, S. P., & Briggs, F. H. (2006). Cosmology at low frequencies: The 21 cm transition and the high-redshift Universe., *433*(4-6), arXiv astro-ph/0608032, 181–301. https://doi.org/10.1016/j.physrep.2006.08.002

Furlanetto, S. R., Zaldarriaga, M., & Hernquist, L. (2004). The Growth of H II Regions During Reionization., *613*(1), arXiv astro-ph/0403697, 1–15. https://doi.org/10.1086/423025

Gao, L., & Theuns, T. (2007). Lighting the Universe with Filaments. *Science*, *317*(5844), arXiv 0709.2165, 1527. https://doi.org/10.1126/science.1146676

Ghara, R., Giri, S. K., Mellema, G., Ciardi, B., Zaroubi, S., Iliev, I. T., Koopmans, L. V. E., Chapman, E., Gazagnes, S., Gehlot, B. K., Ghosh, A., Jelić, V., Mertens, F. G., Mondal, R., Schaye, J., Silva, M. B., Asad, K. M. B., Kooistra, R., Mevius, M., . . . Yatawatta, S. (2020). Constraining the intergalactic medium at z $\approx$ 9.1 using LOFAR Epoch of Reionization observations., arXiv 2002.07195. https://doi.org/10.1093/mnras/staa487

Haiman, Z., Spaans, M., & Quataert, E. (2000). Ly$\alpha$ Cooling Radiation from High-Redshift Halos., *537*(1), arXiv astro-ph/0003366, L5–L8. https://doi.org/10.1086/312754

Harker, G. J. A., Zaroubi, S., Thomas, R. M., Jelić, V., Labropoulos, P., Mellema, G., Iliev, I. T., Bernardi, G., Brentjens, M. A., De Bruyn, A. G., Ciardi, B., Koopmans, L. V. E., Pandey, V. N., Pawlik, A. H., Schaye, J., & Yatawatta, S. (2009). Detection and extraction of signals from the epoch of reionization using higher-order one-point statistics. *Monthly Notices of the Royal Astronomical Society*, *393*(4), https://academic.oup.com/mnras/article-pdf/393/4/1449/3256067/mnras0393-1449.pdf, 1449–1458. https://doi.org/10.1111/j.1365-2966.2008.14209.x

Hutter, A., Watkinson, C. A., Seiler, J., Dayal, P., Sinha, M., & Croton, D. J. (2020). The 21 cm bispectrum during reionization: a tracer of the ionization topology., *492*(1), arXiv 1907.04342, 653–667. https://doi.org/10.1093/mnras/stz3139

Iršič, V., Viel, M., Haehnelt, M. G., Bolton, J. S., Cristiani, S., Becker, G. D., D'Odorico, V., Cupani, G., Kim, T.-S., Berg, T. A. M., López, S., Ellison, S., Christensen, L., Denney, K. D., & Worseck, G. (2017). New constraints on the free-streaming of warm dark matter from intermediate and small scale Lyman-$\alpha$ forest data., *96*(2), arXiv 1702.01764, 023522. https://doi.org/10.1103/PhysRevD.96.023522

Ishiyama, T., Sudo, K., Yokoi, S., Hasegawa, K., Tominaga, N., & Susa, H. (2016). Where are the Low-mass Population III Stars?, *826*(1), arXiv 1602.00465, 9. https://doi.org/10.3847/0004-637X/826/1/9

Kaplinghat, M., Chu, M., Haiman, Z., Holder, G. P., Knox, L., & Skordis, C. (2003). Probing the Reionization History of the Universe using the Cosmic Microwave Background Polarization., *583*(1), arXiv astro-ph/0207591, 24–32. https://doi.org/10.1086/344927

Kennedy, R., Frenk, C., Cole, S., & Benson, A. (2014). Constraining the warm dark matter particle mass with Milky Way satellites. *Monthly Notices of the Royal Astronomical Society*, *442*(3), https://academic.oup.com/mnras/article-pdf/442/3/2487/3537915/stu719.pdf, 2487–2495. https://doi.org/10.1093/mnras/stu719

Kolb, E. W., & Turner, M. S. (1990). *The early universe* (Vol. 69).

Kolopanis, M., Jacobs, D. C., Cheng, C., Parsons, A. R., Kohn, S. A., Pober, J. C., Aguirre, J. E., Ali, Z. S., Bernardi, G., Bradley, R. F., Carilli, C. L., DeBoer, D. R., Dexter, M. R., Dillon, J. S., Kerrigan, J., Klima, P., Liu, A., MacMahon, D. H. E., Moore,

D. F., ... Walker, A. (2019). A Simplified, Lossless Reanalysis of PAPER-64., *883*(2), arXiv 1909.02085, 133. https://doi.org/10.3847/1538-4357/ab3e3a

Komatsu, E., Smith, K. M., Dunkley, J., Bennett, C. L., Gold, B., Hinshaw, G., Jarosik, N., Larson, D., Nolta, M. R., Page, L., Spergel, D. N., Halpern, M., Hill, R. S., Kogut, A., Limon, M., Meyer, S. S., Odegard, N., Tucker, G. S., Weiland, J. L., ... Wright, E. L. (2011). Seven-year Wilkinson Microwave Anisotropy Probe (WMAP) Observations: Cosmological Interpretation., *192*(2), arXiv 1001.4538, 18. https://doi.org/10.1088/0067-0049/192/2/18

Koopmans, L., Pritchard, J., Mellema, G., Aguirre, J., Ahn, K., Barkana, R., van Bemmel, I., Bernardi, G., Bonaldi, A., Briggs, F., de Bruyn, A. G., Chang, T. C., Chapman, E., Chen, X., Ciardi, B., Dayal, P., Ferrara, A., Fialkov, A., Fiore, F., ... Trott, C. (2015). The Cosmic Dawn and Epoch of Reionisation with SKA, In *Advancing Astrophysics with the Square Kilometre Array (AASKA14)*.

Lapi, A., & Danese, L. (2015). Cold or warm? Constraining dark matter with primeval galaxies and cosmic reionization after Planck., *2015*(9), arXiv 1508.02147, 003. https://doi.org/10.1088/1475-7516/2015/09/003

Li, W., Pober, J. C., Barry, N., Hazelton, B. J., Morales, M. F., Trott, C. M., Lanman, A., Wilensky, M., Sullivan, I., Beardsley, A. P., Booler, T., Bowman, J. D., Byrne, R., Crosse, B., Emrich, D., Franzen, T. M. O., Hasegawa, K., Horsley, L., Johnston-Hollitt, M., ... Zheng, Q. (2019). First Season MWA Phase II Epoch of Reionization Power Spectrum Results at Redshift 7., *887*(2), arXiv 1911.10216, 141. https://doi.org/10.3847/1538-4357/ab55e4

Loeb, A., & Barkana, R. (2001). The Reionization of the Universe by the First Stars and Quasars., *39*arXiv astro-ph/0010467, 19–66. https://doi.org/10.1146/annurev.astro.39.1.19

Lovell, M. R., Frenk, C. S., Eke, V. R., Jenkins, A., Gao, L., & Theuns, T. (2014). The properties of warm dark matter haloes., *439*(1), arXiv 1308.1399, 300–317. https://doi.org/10.1093/mnras/stt2431

Madau, P., & Rees, M. J. (2001). Massive Black Holes as Population III Remnants., *551*(1), arXiv astro-ph/0101223, L27–L30. https://doi.org/10.1086/319848

Maio, U., & Viel, M. (2015). The first billion years of a warm dark matter universe., *446*(3), arXiv 1409.6718, 2760–2775. https://doi.org/10.1093/mnras/stu2304

Majumdar, S., Bharadwaj, S., & Choudhury, T. R. (2013). The effect of peculiar velocities on the epoch of reionization 21-cm signal., *434*(3), arXiv 1209.4762, 1978–1988. https://doi.org/10.1093/mnras/stt1144

Majumdar, S., Mellema, G., Datta, K. K., Jensen, H., Choudhury, T. R., Bharadwaj, S., & Friedrich, M. M. (2014). On the use of seminumerical simulations in predicting the 21-cm signal from the epoch of reionization. *Monthly Notices of the Royal Astronomical Society*, *443*(4), http://oup.prod.sis.lan/mnras/article-pdf/443/4/2843/6274877/stu1342.pdf, 2843–2861. https://doi.org/10.1093/mnras/stu1342

Majumdar, S., Pritchard, J. R., Mondal, R., Watkinson, C. A., Bharadwaj, S., & Mellema, G. (2018). Quantifying the non-Gaussianity in the EoR 21-cm signal through bispectrum., *476*(3), arXiv 1708.08458, 4007–4024. https://doi.org/10.1093/mnras/sty535

Mao, Y., Shapiro, P. R., Mellema, G., Iliev, I. T., Koda, J., & Ahn, K. (2012). Redshift-space distortion of the 21-cm background from the epoch of reionization - I. Methodology re-examined., *422*(2), arXiv 1104.2094, 926–954. https://doi.org/10.1111/j.1365-2966.2012.20471.x

Mellema, G., Koopmans, L., Shukla, H., Datta, K. K., Mesinger, A., & Majumdar, S. (2015). HI tomographic imaging of the Cosmic Dawn and Epoch of Reionization with SKA.

Mertens, F. G., Mevius, M., Koopmans, L. V. E., Offringa, A. R., Mellema, G., Zaroubi, S., Brentjens, M. A., Gan, H., Gehlot, B. K., Pand ey, V. N., Sardarabadi, A. M., Vedantham, H. K., Yatawatta, S., Asad, K. M. B., Ciardi, B., Chapman, E., Gazagnes, S., Ghara, R., Ghosh, A., . . . Silva, M. B. (2020). Improved upper limits on the 21 cm signal power spectrum of neutral hydrogen at $z \approx 9.1$ from LOFAR., *493*(2), arXiv 2002.07196, 1662–1685. https://doi.org/10.1093/mnras/staa327

Mesinger, A., Furlanetto, S., & Cen, R. (2011). 21CMFAST: a fast, seminumerical simulation of the high-redshift 21-cm signal., *411*(2), arXiv 1003.3878, 955–972. https://doi.org/10.1111/j.1365-2966.2010.17731.x

Mo, H., van den Bosch, F. C., & White, S. (2010). *Galaxy Formation and Evolution*.

Mondal, R., Bharadwaj, S., & Majumdar, S. (2017). Statistics of the epoch of reionization (EoR) 21-cm signal - II. The evolution of the power-spectrum error-covariance., *464*(3), arXiv 1606.03874, 2992–3004. https://doi.org/10.1093/mnras/stw2599

Paciga, G., Albert, J. G., Bandura, K., Chang, T.-C., Gupta, Y., Hirata, C., Odegova, J., Pen, U.-L., Peterson, J. B., Roy, J., Shaw, J. R., Sigurdson, K., & Voytek, T. (2013). A simulation-calibrated limit on the H I power spectrum from the GMRT Epoch of Reionization experiment., *433*(1), arXiv 1301.5906, 639–647. https://doi.org/10.1093/mnras/stt753

Pillepich, A., Porciani, C., & Matarrese, S. (2007). The Bispectrum of Redshifted 21 Centimeter Fluctuations from the Dark Ages., *662*(1), arXiv astro-ph/0611126, 1–14. https://doi.org/10.1086/517963

Planck Collaboration, Ade, P. A. R., Aghanim, N., Arnaud, M., Ashdown, M., Aumont, J., Baccigalupi, C., Banday, A. J., Barreiro, R. B., Bartlett, J. G., Bartolo, N., Battaner, E., Battye, R., Benabed, K., Benoıt, A., Benoit-Lévy, A., Bernard, J. .-.-P., Bersanelli, M., Bielewicz, P., . . . Zonca, A. (2016). Planck 2015 results. XIII. Cosmological parameters., *594*arXiv 1502.01589, A13. https://doi.org/10.1051/0004-6361/201525830

Press, W. H., & Schechter, P. (1974). Formation of Galaxies and Clusters of Galaxies by Self-Similar Gravitational Condensation., *187*, 425–438. https://doi.org/10.1086/152650

Primack, J. R. (2009). Cosmology: small-scale issues. *New Journal of Physics*, *11*(10), arXiv 0909.2247, 105029. https://doi.org/10.1088/1367-2630/11/10/105029

Pritchard, J. R., & Furlanetto, S. R. (2006). Descending from on high: Lyman-series cascades and spin-kinetic temperature coupling in the 21-cm line., *367*(3), arXiv astro-ph/0508381, 1057–1066. https://doi.org/10.1111/j.1365-2966.2006.10028.x

Ricotti, M., & Ostriker, J. P. (2004). X-ray pre-ionization powered by accretion on the first black holes - I. A model for the WMAP polarization measurement., *352*(2), arXiv astro-ph/0311003, 547–562. https://doi.org/10.1111/j.1365-2966.2004.07942.x

Rivera-Thorsen, T. E., Dahle, H., Chisholm, J., Florian, M. K., Gronke, M., Rigby, J. R., Gladders, M. D., Mahler, G., Sharon, K., & Bayliss, M. (2019). Gravitational lensing reveals ionizing ultraviolet photons escaping from a distant galaxy. *Science*, *366*(6466), arXiv 1904.08186, 738–741. https://doi.org/10.1126/science.aaw0978

Roszkowski, L., Sessolo, E. M., & Trojanowski, S. (2018). WIMP dark matter candidates and searches—current status and future prospects. *Reports on Progress in Physics*, *81*(6), arXiv 1707.06277, 066201. https://doi.org/10.1088/1361-6633/aab913

Safarzadeh, M., Scannapieco, E., & Babul, A. (2018). A Limit on the Warm Dark Matter Particle Mass from the Redshifted 21 cm Absorption Line. *The Astrophysical Journal*, *859*(2), L18. https://doi.org/10.3847/2041-8213/aac5e0

Schneider, A. (2012). *Dark matter structures and the free streaming scale* (Doctoral dissertation). University of Zurich. https://doi.org/10.5167/uzh-75587

Schneider, A., Smith, R. E., Macciò, A. V., & Moore, B. (2012). Non-linear evolution of cosmological structures in warm dark matter models., *424*(1), arXiv 1112.0330, 684–698. https://doi.org/10.1111/j.1365-2966.2012.21252.x

Schneider, A., Smith, R. E., & Reed, D. (2013). Halo mass function and the free streaming scale., *433*(2), arXiv 1303.0839, 1573–1587. https://doi.org/10.1093/mnras/stt829

Shimabukuro, H., Yoshiura, S., Takahashi, K., Yokoyama, S., & Ichiki, K. (2016). 21 cm line bispectrum as a method to probe cosmic dawn and epoch of reionization. *Monthly Notices of the Royal Astronomical Society*, *458*(3), https://academic.oup.com/mnras/article-pdf/458/3/3003/8006770/stw482.pdf, 3003–3011. https://doi.org/10.1093/mnras/stw482

Singh, S., Subrahmanyan, R., Udaya Shankar, N., Sathyanarayana Rao, M., Fialkov, A., Cohen, A., Barkana, R., Girish, B. S., Raghunathan, A., Somashekar, R., & Srivani, K. S. (2018). SARAS 2 Constraints on Global 21 cm Signals from the Epoch of Reionization., *858*(1), arXiv 1711.11281, 54. https://doi.org/10.3847/1538-4357/aabae1

Sitwell, M., Mesinger, A., Ma, Y.-Z., & Sigurdson, K. (2014). The imprint of warm dark matter on the cosmological 21-cm signal., *438*(3), arXiv 1310.0029, 2664–2671. https://doi.org/10.1093/mnras/stt2392

Smith, R. E., & Markovic, K. (2011). Testing the warm dark matter paradigm with large-scale structures., *84*(6), arXiv 1103.2134, 063507. https://doi.org/10.1103/PhysRevD.84.063507

Songaila, A., & Cowie, L. L. (2010). THE EVOLUTION OF LYMAN LIMIT ABSORPTION SYSTEMS TO REDSHIFT SIX. *The Astrophysical Journal*, *721*(2), 1448–1466. https://doi.org/10.1088/0004-637x/721/2/1448

Springel, V. (2005). The cosmological simulation code GADGET-2., *364*(4), arXiv astro-ph/0505010, 1105–1134. https://doi.org/10.1111/j.1365-2966.2005.09655.x

Steidel, C. C., Pettini, M., & Adelberger, K. L. (2001). Lyman-Continuum Emission from Galaxies at Z $\sim$= 3.4., *546*(2), arXiv astro-ph/0008283, 665–671. https://doi.org/10.1086/318323

Thomas, R. M., & Zaroubi, S. (2008). Time-evolution of ionization and heating around first stars and miniqsos., *384*(3), arXiv 0709.1657, 1080–1096. https://doi.org/10.1111/j.1365-2966.2007.12767.x

Viel, M., Becker, G. D., Bolton, J. S., & Haehnelt, M. G. (2013). Warm dark matter as a solution to the small scale crisis: New constraints from high redshift Lyman-$\alpha$ forest data., *88*(4), arXiv 1306.2314, 043502. https://doi.org/10.1103/PhysRevD.88.043502

Viel, M., Lesgourgues, J., Haehnelt, M. G., Matarrese, S., & Riotto, A. (2005). Constraining warm dark matter candidates including sterile neutrinos and light gravitinos with WMAP and the Lyman-$\alpha$ forest., *71*(6), arXiv astro-ph/0501562, 063534. https://doi.org/10.1103/PhysRevD.71.063534

Villanueva-Domingo, P., Gnedin, N. Y., & Mena, O. (2018). Warm Dark Matter and Cosmic Reionization., *852*(2), arXiv 1708.08277, 139. https://doi.org/10.3847/1538-4357/aa9ff5

Watkinson, C. A. [C. A.], Mesinger, A., Pritchard, J. R., & Sobacchi, E. (2015). 21-cm signatures of residual Hi inside cosmic Hii regions during reionization. *Monthly Notices of the Royal Astronomical Society*, *449*(3), 3202–3211. https://doi.org/10.1093/mnras/stv499

Watkinson, C. A. [Catherine A], Giri, S. K., Ross, H. E., Dixon, K. L., Iliev, I. T., Mellema, G., & Pritchard, J. R. (2018). The 21-cm bispectrum as a probe of non-Gaussianities due to X-ray heating. *Monthly Notices of the Royal Astronomical Society*, *482*(2), https://academic.oup.com/mnras/article-pdf/482/2/2653/26853752/sty2740.pdf, 2653–2669. https://doi.org/10.1093/mnras/sty2740

Weinberg, D. H., Bullock, J. S., Governato, F., Kuzio de Naray, R., & Peter, A. H. G. (2015). Cold dark matter: Controversies on small scales. *Proceedings of the National Academy of Science*, *112*(40), arXiv 1306.0913, 12249–12255. https://doi.org/10.1073/pnas.1308716112

White, R. L., Becker, R. H., Fan, X., & Strauss, M. A. (2003). Probing the Ionization State of the Universe at z>6., *126*(1), arXiv astro-ph/0303476, 1–14. https://doi.org/10.1086/375547

Wouthuysen, S. A. (1952). On the excitation mechanism of the 21-cm (radio-frequency) interstellar hydrogen emission line., *57*, 31–32. https://doi.org/10.1086/106661

Yoshida, N., Abel, T., Hernquist, L., & Sugiyama, N. (2003). Simulations of Early Structure Formation: Primordial Gas Clouds., *592*(2), arXiv astro-ph/0301645, 645–663. https://doi.org/10.1086/375810

Yoshida, N., Bromm, V., & Hernquist, L. (2004). The Era of Massive Population III Stars: Cosmological Implications and Self-Termination., *605*(2), arXiv astro-ph/0310443, 579–590. https://doi.org/10.1086/382499

Zahn, O., Mesinger, A., McQuinn, M., Trac, H., Cen, R., & Hernquist, L. E. (2011). Comparison of reionization models: radiative transfer simulations and approximate, seminumeric models., *414*(1), arXiv 1003.3455, 727–738. https://doi.org/10.1111/j.1365-2966.2011.18439.x